Transient DNA Binding Induces RNA Polymerase II Compartmentalization During Herpesviral Infection Distinct From Phase Separation

David T McSwiggen[1,2], Anders S Hansen[1,2], Hervé Marie-Nelly[1,2], Sheila Teves[1,3], Alec B Heckert[1,2] , Claire Dugast-Darzacq[1,2], Yvonne Hao[1], Kayla K Umemoto[1], Robert Tjian[1,4,*], Xavier Darzacq[1,2,*]

[1]Department of Molecular and Cell Biology, University of California Berkeley, CA, USA, 94720
[2]California Institute of Regenerative Medicine Center of Excellence, University of California Berkeley, CA, USA, 94720
[3]Department of Biochemistry and Molecular Biology, University of British Columbia, Vancouver, BC, Canada, BC V6T 1Z4
[4]Howard Hughes Medical Institute, University of California Berkeley, CA, USA, 94720

*To whom correspondence should be addressed:
Robert Tjian, jmlim@berkeley.edu
Xavier Darzacq, darzacq@berkeley.edu

Summary

During lytic infection, Herpes Simplex Virus 1 generates replication compartments (RCs) in host nuclei that efficiently recruit protein factors, including host RNA Polymerase II (Pol II). Pol II and other cellular factors form hubs in uninfected cells that are proposed to phase separate via multivalent protein-protein interactions mediated by their intrinsically disordered regions. Using a battery of live cell microscopic techniques, we show that although RCs superficially exhibit many characteristics of phase separation, the recruitment of Pol II instead derives from nonspecific interactions with the viral DNA. We find that the viral genome remains nucleosome-free, profoundly affecting the way Pol II explores RCs by causing it to repetitively visit nearby binding sites, thereby creating local Pol II accumulations. This mechanism, distinct from phase separation, allows viral DNA to outcompete host DNA for cellular proteins. Our work provides new insights into the strategies used to create local molecular hubs in cells.

Article Keywords: Transcription, Phase Separation, Nuclear Organization, Single Particle Tracking, RNA Polymerase II, Herpesvirus, Microscopy

Introduction

The ability to control the local concentration of molecules within cells is fundamental to living organisms. A classic example is the use of electrochemical gradients across membranes to facilitate cellular work. In recent years, our understanding of the forces driving the formation of sub-nuclear compartments has undergone a paradigm shift. A number of studies suggest that many proteins have the ability to spontaneously form separated liquid phases *in vitro* (Hyman et al., 2014), and recent work highlights the possibility that similar liquid compartments may occur *in vivo* (Shin et al., 2017; Strom et al., 2017). Such liquid-liquid demixing has been proposed to be a common mechanism to sequester specific macromolecules within a compartment, or to increase their local concentration to facilitate chemical interactions. Formation of these structures is thought to be predominantly driven by weak, multivalent protein:protein interactions mediated by intrinsically disordered regions (IDRs), which are often comprised of low complexity polypeptides, and sometimes aided by the presence of modular RNA or DNA binding motifs (Banani et al., 2017; Hyman et al., 2014).

These observations have opened new frontiers of inquiry in cell biology, and generated a deeper appreciation for the diversity of mechanisms that a cell may deploy to locally concentrate certain molecular components. The list of proteins—particularly nuclear proteins—that can undergo phase separation *in vitro* continues to grow (Courchaine et al., 2016). For example, recent studies of RNA Polymerase II (Pol II) and its regulators have shown that Pol II forms dynamic hubs whose size are dependent on the number of intrinsically disordered heptad peptide repeats contained within the C-terminal domain (CTD) (Boehning et al., 2018), and that various CTD interacting factors may form phase separated droplets in vitro (Lu et al., 2018). Even so, it remains unclear which molecular interactions drive the formation of domains via liquid-liquid phase separation (LLPS), or many different classes of interactions mediate such local molecular behavior (Chong et al., 2018). Importantly, we do not we fully understand the nature of the molecular forces that drive compartmentalization *in vivo,* still lack compelling evidence to establish the functional consequences of these compartments for the biological activities of their constituents.

Herpes Simplex Virus type 1 (HSV1) provides an attractive system to study this question because of its ability to form compartments in the nucleus of infected cells *de novo*. HSV1 is a common human pathogen that hijacks its host's transcription machinery during lytic infection (Rice et al., 1994). Transcription of HSV1 genes occurs in three waves: immediate early, early, and late, with the latter strictly occurring only after the onset of viral DNA replication (Knipe and Cliffe, 2008). Like many DNA viruses, HSV1 creates subcellular structures called replication compartments (RC) where both viral and host factors congregate to direct replication of the viral genome, continue viral transcription, and assemble new virions (Schmid et al., 2014). Recent reports highlight the ability of HSV1 to usurp host Pol II to transcribe its own genome such that, once late gene transcription commences, the host chromatin is largely devoid of productively transcribing Pol II, and the majority of newly synthesized mRNAs are viral in origin (Abrisch et al., 2015; Rutkowski et al., 2015). Consistent with genomic data, immunofluorescence staining of infected cells shows a dramatic enrichment of Pol II and other nuclear factors in RCs (Rice et al., 1994).

Given this shift in both the sub-nuclear localization of Pol II upon infection, and its effect on the transcriptional output of an infected cell, we chose to examine the mechanism of Pol II recruitment to HSV1 RCs as a model case for the generation of new subcellular compartments. We employed a combination of imaging approaches, including live cell single particle tracking

81 (SPT), fluorescence loss in photobleaching (FLIP), and fluorescence recovery after
82 photobleaching (FRAP), in addition to single molecule localization microscopy to probe Pol II
83 localization and behavior within RCs. We complemented these imaging assays with genetic and
84 chemical perturbation experiments while measuring Pol II behavior in infected and uninfected
85 cells. Finally, we performed ATAC-seq to sample the chromatin state of the viral DNA, and used
86 Oligopaints to estimate the number of viral genomes within the RCs of infected cells.
87 Despite initial experiments showing that RCs display many of the macroscopic hallmarks of
88 LLPS, we unexpectedly found that recruitment of Pol II and other DNA-binding proteins to RCs
89 is achieved through a distinct compartmentalization mechanism not driven by IDR-dependent
90 protein:protein interactions. Rather, we find that Pol II recruitment is achieved predominantly
91 through transient, nonspecific binding of Pol II to viral DNA. These interactions occur
92 independent of transcription initiation, and rely on the unusual feature of the HSV1 genome that
93 it is largely maintained as "naked", nucleosome-free DNA, which is much more accessible to
94 DNA-binding proteins than host chromatin. Our findings show that nonspecific binding can play
95 a key role in RC formation, in Pol II recruitment during infection, and more generally in the
96 repertoire of distinct mechanisms a cell might employ to generate nuclear compartments.

97 **Results**

98 **Pol II recruitment to Replication Compartments exhibits hallmarks of liquid-liquid**
99 **demixing**

100 HSV1 RCs form *de novo* following lytic infection, making them an attractive system to
101 dissect compartment formation at the molecular level. To determine the mechanisms leading to
102 the hijacking of Pol II, we used a U2OS cell line in which the catalytic subunit of Pol II has been
103 fused to HaloTag (Boehning et al., 2018; Los et al., 2008). HSV1 infection occurs rapidly, with
104 large replication compartments (RCs) forming within a few hours (Figure 1A). Because we were
105 most interested in the early stages of lytic infection when Pol II is actively recruited to the RC,
106 we focused our experiments on the period between 3 hours post infection (hpi) when RCs begin
107 to emerge, and 6 hpi when infected cells begin to display significant cytopathic effects (Movies
108 S1 and S2). To capture the earliest stages of Pol II recruitment, we used a low multiplicity of
109 infection (MOI) to obtain a minimal dose of virions per cell.
110 In addition to Pol II, many other viral and nuclear factors re-localize to RCs (Dembowski and
111 DeLuca, 2015). In fact, this redistribution of proteins is so dramatic that it can be seen by phase
112 contrast microscopy as a change in the refractive index of RCs (Figure 1A). We observed, in
113 agreement with previous studies, that RCs grow and move over the course of infection (Figure
114 1B) (Chang et al., 2011; Taylor et al., 2003). We also found that RCs exhibit several other
115 behaviors characteristic of liquid droplets, such as an ability to fuse (Figure 1B, Movies S1 and
116 S2) and a spherical shape, as indicated by an aspect ratio close to one (Figure 1C, median 1.18, n
117 = 817). RCs are particularly round early in infection, when they are small (Figure S1). Such
118 behaviors closely mimic the behavior of phase-separated liquid droplets, where the interface is
119 thought to be subject to surface tension (Brangwynne et al., 2011; Feric et al., 2016).
120 Because LLPS is thought to be mostly driven by weak protein:protein interactions between
121 intrinsically disordered regions (IDRs), we used the protein disordered region prediction
122 algorithm IUPred to predict IDRs within viral proteins (IUPred > 0.55) (Dosztanyi et al., 2005;
123 Dosztányi et al., 2005), and found these predictions match well with known disordered regions
124 (Figure 1D) (Everett, 2000; Hew et al., 2015; Pfoh et al., 2015; Tunnicliffe et al., 2015). Across

125 all viral proteins, we identified predicted IDRs longer than 10 amino acids, and used these to
126 estimate what fraction of each protein sequence is unstructured (Figure 1E, Table S1). When
127 categorized by temporal class, we noted that the immediate early (IE) and viral tegument
128 proteins—the two groups that are presented to the cell first upon infection—had the highest
129 fraction of predicted intrinsic disorder. In fact, when compared to a list of proteins known to
130 undergo LLPS *in vitro*, the IE and tegument proteins are slightly more disordered (Figure 1E;
131 Table S2 and citations within). Under the working hypothesis that multivalent interactions
132 between protein IDRs drive phase separation, the similarity in predicted disorder profiles
133 between this curated list and the IE and tegument proteins suggests that IDRs in viral proteins are
134 as likely to drive LLPS as experimentally validated proteins.
135 Based on the above descriptive observations, we hypothesized that Pol II is recruited to RCs
136 through interactions between its CTD and other IDR-containing proteins within the RC. To test
137 this, we measured the FRAP dynamics of Pol II in RCs. We saw a consistent slowing of recovery
138 as infection progressed and RCs got larger (Figure 1F), which could be interpreted as evidence
139 that RCs act as a separate liquid phase that incorporates Pol II and sequesters it from the rest of
140 the nucleoplasm. Subsequent experiments to directly test this hypothesis, however, cast doubt on
141 this interpretation.
142 We recently reported that hub formation by Pol II in uninfected cells occurs in a manner
143 dependent on the length of the Pol II CTD (Boehning et al., 2018). To test whether the Pol II
144 CTD likewise mediates interaction with RCs, we compared Pol II accumulation in RCs in cells
145 with the wild-type Pol II CTD (with 52 heptad repeats) and cell lines bearing truncated (25
146 repeats) or extended (70 repeats) CTDs. To our surprise, the length of the CTD had no detectable
147 effect on its incorporation into RCs (Figure 1G), suggesting that Pol II does not require IDR
148 interactions through its CTD to become enriched.
149 As a further test of the role of IDR interactions in Pol II accumulation in RCs, we treated
150 cells with 1,6-hexanediol, which disrupts weak hydrophobic interactions between IDRs that
151 drive LLPS (Boehning et al., 2018; Chong et al., 2018; Lin et al., 2016; Lu et al., 2018; Strom et
152 al., 2017). We infected cells for five hours, and then subjected them to treatment with a high
153 concentration (10% v/v) of 1,6-hexanediol for one, five, or ten minutes. Five minutes after
154 treatment, the morphology of the nucleus began to change, and by ten minutes it was noticeably
155 deformed, consistent with widespread disruption of cellular organization by 1,6-hexanediol (Lin
156 et al., 2016). Nonetheless, Pol II remained highly enriched in RCs after 1,6-hexanediol treatment
157 (Figure 1H), implying that formation of RCs does not require interactions between IDRs of Pol II
158 and viral proteins.

159 **Pol II diffusion within and across RC boundaries is inconsistent with an LLPS model**

160 The data outlined in Figure 1 present a potential contradiction, as RCs exhibit several
161 properties commonly associated with phase separation *in vitro*, yet Pol II recruitment to RCs was
162 not susceptible to disruption by 1,6-hexanediol or dependent on CTD length. Given these results,
163 we sought to better understand the mechanism driving the enrichment of Pol II in RCs by
164 measuring the behavior of individual Pol II molecules. To accurately capture both immobile and
165 freely diffusing Pol II molecules, we used stroboscopic photo-activatable single particle tracking
166 (spaSPT) to visualize and track molecules (Figure 2A) (Hansen et al., 2017, 2018). We labeled
167 HaloTag-Pol II with equal amounts of JF_{549} and PA-JF_{646} (Grimm et al., 2015, 2016), which
168 allowed us to monitor its overall distribution using the former dye while tracking individual
169 molecules using the latter dye. We generated masks of the location of the nuclear periphery and

170 individual RCs and used these masks to sort trajectories as either "inside" or "outside" of RCs
171 (Figure 2B).
172 Quantitative measurements can be made by building histograms of all the displacement
173 distances from the trajectories and fitting to a two-state model in which Pol II can either be freely
174 diffusing ("free"), or immobile and hence presumably bound to DNA ("bound") (Figure 2C).
175 Such a two-state model gives two important pieces of information: the fraction of "bound" and
176 "free" molecules, and the apparent diffusion coefficient of each population (Hansen et al., 2018).
177 It is important to note that, because this modeling approach takes the aggregate of many
178 thousands of molecules, these data cannot measure how long a particular molecule remains
179 bound in a given binding event. Here, "bound" refers to both specific DNA binding events—e.g.
180 molecules assembled at a promoter or engaged in mRNA elongation—as well as transient,
181 nonspecific binding interactions.
182 The difference in the behavior of Pol II inside of RCs compared with the rest of the
183 nucleoplasm is immediately apparent from examining the lengths of jumps between consecutive
184 frames (Figure 2D). Fitting a two-state model to the data, we were surprised to find that the mean
185 apparent diffusion coefficient of the free population was unchanged between trajectories inside
186 of RCs compared with those outside RCs or in uninfected cells. If RCs were a *bona fide* separate
187 phase, one would expect differences in molecular crowding or intermolecular interactions to
188 predominantly affect free diffusion, resulting in substantially different diffusion coefficients
189 between the populations (Bergeron-Sandoval et al., 2016). Furthermore, the similarity in
190 diffusion coefficients between infected and uninfected cells argues against a separate viral
191 protein-Pol II complex responsible for recruitment to RCs.
192 We verified this result in two ways: First, we performed a fluorescence loss in
193 photobleaching (FLIP) experiment, in which a strong bleaching laser targets the inside of an RC
194 and loss of fluorescence elsewhere in the nucleus is measured to quantify exchange of Pol II
195 between the nucleoplasm and the RC. Consistent with the spaSPT data, we see that Pol II
196 molecules exchange between RCs and the rest of the nucleoplasm as fast, if not faster, than Pol II
197 in an uninfected cell (Figure 2F). Similar results were obtained by using Pol II tagged with the
198 photo-convertible fluorescent protein Dendra2 (Cisse et al., 2013) and photo-converting, rather
199 than bleaching, molecules in the RC (Figure S2). Thus, Pol II molecules diffuse out of the RC,
200 rather than remaining sequestered within a single compartment. Second, a liquid-liquid phase
201 separation model predicts that a diffusing Pol II molecule within an RC will be more likely to
202 remain within the RC than to exit the RC when it reaches the compartment boundary. To test this
203 prediction, we examined all trajectories for events in which a molecule crosses from inside of the
204 RC to outside, or vice versa, to look for evidence of such a constraint. Comparing the
205 distribution of displacements for a particle going from inside the RC to outside, we see no
206 difference in the distribution of displacements, either entering or leaving RCs, when compared to
207 uninfected cells in which mock RC annotations were randomly imposed *in silico* (Figure 2G,
208 Figure S3). With these experiments we cannot detect any evidence of a boundary for molecules
209 entering or leaving RCs, further arguing that this compartment does not consist of a distinct
210 liquid phase.
211 While the two-state model shows no change in diffusion coefficient of molecules inside
212 versus outside RCs, the fraction of molecules in the "bound" state nearly doubles inside RCs,
213 reaching ~70% (Figure 2H). The diffusion coefficients we measured with the bound populations
214 are still consistent with those of chromatin (Hansen et al., 2018), indicative that these
215 populations reflect DNA binding (Figure S4). The increase in the fraction of bound molecules is

216 further supported by the FRAP data (Figure 1F). We verified this was not an artifact of the
217 masking process by using the same process of artificially imposing RCs randomly *in silico*
218 (Figure S3), and we found no difference in the fraction of bound molecules. Such a significant
219 shift in the relative populations of bound and free molecules inside RCs, taken together with the
220 previous data, shows that the mechanism driving Pol II recruitment to RCs is dominated by DNA
221 binding, rather than by IDR-mediated interactions that sequester Pol II away in a separate liquid
222 phase.

223 **Pol II recruitment to RCs occurs independent of transcription initiation**

224 The above data argue against formation of RCs by LLPS, suggesting that some other
225 mechanism must explain the doubling of DNA-bound Pol II in RCs. One possibility is that
226 increased recruitment of Pol II is explained by high levels of active transcription within RCs.
227 Multiple lines of evidence suggest that transcription derived from the viral genome is activated to
228 a much greater extent than even the most highly transcribed host mRNA (Rutkowski et al., 2015)
229 and so an enriched population of actively elongating Pol II would be expected to increase the
230 "bound" population.

231 To test whether active transcription is necessary for Pol II recruitment to RCs, we treated
232 infected cells with either Flavopiridol or Triptolide, two small molecules that selectively inhibit
233 different stages of transcription initiation (Figure 3A). Flavopiridol is a potent inhibitor of CDK9
234 that prevents the phosphorylation of serine-2 of the RPB1 CTD heptad, and thus prevents
235 transcription from proceeding beyond ~50 nucleotides downstream of the transcription start site
236 (TSS) (Chao and Price, 2001; Jonkers et al., 2014). Triptolide, on the other hand, is an inhibitor
237 of the ATPase domain of TFIIH, preventing the stable engagement of Pol II at the Pre-Initiation
238 Complex (PIC) (Alekseev et al., 2017; Chen et al., 2015; Titov et al., 2011). Samples treated
239 with Triptolide show a loss of engaged Pol II at promoters (Jonkers et al., 2014; Shao and
240 Zeitlinger, 2017).

241 HSV1 RCs require the expression of immediate-early and early genes to generate the DNA
242 replication machinery, so we allowed the infection to progress for four hours before treating with
243 either compound. Cells at this timepoint have well formed RCs, and Pol II binding is already
244 greatly increased (Figure 2H). We treated these cells with 1 μM Flavopiridol or 1 μM Triptolide
245 for 15, 30, or 45 minutes to allow any elongating polymerases to finish transcribing (Figure 3B).
246 After treatment, we fixed cells, and we performed RNA fluorescence in situ hybridization
247 (FISH) using a probe against an intronic region to detect nascent transcripts and, in parallel, and
248 immunofluorescence to mark the DNA-binding protein ICP8, a common marker for RCs (Taylor
249 et al., 2003). After 30 minutes of drug treatment, transcription is significantly reduced (Figure
250 S5). Remarkably, even after 45 minutes of treatment, ~80% of the Pol II signal remains within
251 RCs (Figure 3C, Figure S5). These data suggest that the recruitment of Pol II to RCs occurs
252 largely independently of transcription, or even stable engagement with gene promoters.

253 We next tested whether treatment with these transcription inhibitors would change the bound
254 fraction measured by spaSPT. In uninfected cells, Triptolide or Flavopiridol treatment both
255 reduce the fraction of bound Pol II by half, to ~15% (Figure 3D), similar to what others have
256 reported (Boehning et al., 2018; Teves et al., 2018). Surprisingly, inhibition of transcription with
257 Flavopiridol reduced the bound fraction inside of RCs by only ~5% (Figure 3D). Even treatment
258 with Triptolide, which prevents stable engagement with TSS-proximal DNA only reduced the
259 fraction bound by ~12% (Figure 3D). We were surprised to see that with either drug treatment,
260 HSV1 infection appears to also confer some resistance to the effects of the drugs on Pol II
261 binding to host chromatin, despite the fact that these concentrations of transcription inhibitors are

262 sufficient to prevent new transcription (Figure 3D, Figure S5). Given the inherent limitation of
263 spaSPT for inferring the length of binding events, we wanted to confirm that drug treatment
264 prevented stable Pol II binding. Indeed, FRAP experiments in infected cells treated with
265 Triptolide show a dramatically faster recovery rate (Figure 2E). For the infected samples, this
266 means that the "bound" molecules measured by SPT do not remain bound for long times, as one
267 would expect from high affinity protein-protein or protein-DNA interactions at cognate sites.
268 Instead, these binding events are likely short compared to the timescales of PIC assembly and
269 transcription initiation. Such highly transient binding events also argue against sequence specific,
270 high affinity interactions as drivers for sequestering Pol II to the RC. The fact that infected cells
271 show resistance, in terms of DNA binding, to the drug treatment may be a result of other viral
272 mechanisms that occur during infection, such as aberrant Pol II CTD phosphorylation (Rice et
273 al., 1994) or termination defects (Rutkowski et al., 2015). Still, our results suggest that viral
274 DNA and/or DNA-associated proteins mediate very rapid, predominantly nonspecific,
275 interactions within RCs.

276 **HSV1 DNA is more accessible than host chromatin to Pol II**

277 The result that Pol II molecules remain bound—however transiently—to the viral DNA, even
278 in the absence of transcription, suggests that the DNA itself likely plays a dominant role in Pol II
279 enrichment in RCs. To our knowledge, the genome copy number present in individual RCs has
280 never been determined, but this information is crucial to understand the role viral DNA may play
281 in RC formation and function. We therefore sought to measure the amount of DNA in RCs using
282 Oligopaints, a variant of DNA fluorescence in situ hybridization, to target fluorescent probes to
283 two specific regions of the viral genome (Figure 4A) (Beliveau et al., 2012; Boettiger et al.,
284 2016). Infected cells were fixed three, four, five, and six hours post infection. The amount of
285 DNA was measured by fluorescence intensity of the compartment, determined independently for
286 the two probe sets. These fluorescence intensities were compared to samples that were infected
287 in the presence of phosphonoacetic acid (PAA), a compound that prevents replication of the viral
288 DNA and thus ensures that there is one copy of the viral genome per punctum (Figure 4B)
289 (Eriksson and Schinazi, 1989).

290 While there is a great deal of expected RC-to-RC heterogeneity, the number of genomes
291 within an RC correlates well with the time post infection (Figure 4C). There is also a strong
292 correlation between RC size and genome copy number (Figure S6). Based on these data, we
293 calculate that the average RC at 6 hpi has a DNA concentration of 3.9×10^4 bp/μm^3,
294 approximately 240 times less concentrated than average host chromatin. The sum of all RCs in
295 an average infected cell corresponds to just ~0.2% of total DNA in karyotypically normal human
296 nuclei (Table S3). Despite being orders of magnitude lower in DNA content and concentration,
297 inhibition of viral DNA replication with PAA caused a ~20% decrease in the fraction of bound
298 Pol II molecules inside the pre-replication foci as measured by spaSPT, nearly down to the level
299 of host chromatin (Figure 4D). This, despite the fact that all immediate early and early genes,
300 including many of the proteins known to interact with Pol II, are still highly expressed in PAA-
301 treated samples (Lester and DeLuca, 2011; Zhou and Knipe, 2002).

302 Since most of the Pol II binding events that we observe inside of an RC appear to be
303 unrelated to transcription, but clearly dependent on viral DNA replication, we wondered what
304 might be different about the viral genome relative to host chromosomes. A likely candidate is the
305 chromatin state of the viral DNA. There is presently no clear consensus about the organization of
306 viral DNA during lytic infection. Multiple studies have successfully used ChIP to sample histone
307 marks to determine histone association with the viral DNA (Bloom et al., 2010; Lang et al.,

308 2017; Lee et al., 2016), though this may also be explained by formation of nonnucleosomal
309 histone-DNA intermediates (Torigoe et al., 2011), especially since mass spectrometry studies
310 have failed to detect histones associated with viral DNA (Dembowski and DeLuca, 2015; Taylor
311 and Knipe, 2004). Moreover, immunofluorescence against histones shows no detectable signal in
312 RCs (Dembowski and DeLuca, 2015). In addition, one function of viral ICP0 is to actively evict
313 histones from DNA, which suggests that the HSV1 genome is maintained largely free of histones
314 (Lee et al., 2016).
315 To test histone occupancy of the viral DNA, and get a measure of its accessibility, we turned
316 to ATAC-seq, which gives signal proportional to the accessibility of the DNA at a given locus
317 (Buenrostro et al., 2013). We infected our HaloTag-Pol II cell line, and performed Tn5
318 transposition reactions at 2, 4, and 6 hpi. We also included a sample that was uninfected, and one
319 infected in the presence of PAA. At all times after infection, the distribution of fragment lengths
320 mapping to the viral genome showed a much faster decay, and no evidence of nucleosomal
321 laddering, in contrast to reads that map to the host genome (Figure 4E, Figure S7). When we
322 visualized the reads along the viral genome, the profiles were strikingly flat and featureless,
323 suggesting that all regions of the viral genome are equally accessible to Tn5 (Figure 4F).
324 Based on the amount of viral DNA present in an infected cell, we calculated the fraction of
325 reads one would expect to map to the virus relative to the host. At 6 hpi, under our infection
326 conditions, viral DNA represents an average 0.2% of total nuclear DNA content. Yet, at this time
327 point, 24.2% of reads mapped to the virus on average. From this, we calculate that DNA inside
328 of RCs is two orders of magnitude more accessible, despite its overall lower DNA concentration
329 relative to host DNA (Table S3).
330 In metazoan genomes, active genes can be identified by their high accessibility (Thurman et
331 al., 2012). An average of all annotated human mRNA genes, centered at the TSS, shows a
332 characteristic peak of accessibility at the TSS for reads with a length corresponding to inter-
333 nucleosomal distances (<100 bp), and a characteristic trough of mononucleosome sized
334 fragments (180 – 250 bp) (Figure 4G). By contrast, TSS averages mapped to the viral genome
335 for either short or mono-nucleosome fragments show no changes in accessibility. Thus, even
336 averaging over all viral transcripts, it is clear that the entire viral DNA remains equally
337 accessible (Figure 4H). Taken together, these data indicate that the HSV genome is maintained in
338 a largely nucleosome-free state and thus, highly accessible to DNA binding proteins such as Pol
339 II.

340 **Transient DNA-protein interactions drive Pol II hub formation through repetitive**
341 **exploration of the replication compartment**

342 Knowing that the DNA inside RCs is vastly more accessible to nuclear factors than the host
343 chromatin, we next asked what emergent properties of this accessible DNA might help explain
344 Pol II recruitment. We took advantage of a viral strain that is able to incorporate chemically
345 modified nucleotides during replication (Dembowski and DeLuca, 2015), to label newly
346 replicated viral DNA with Alexa Fluor 647, and thus allow DNA in the RCs to be visualized at
347 high resolution using stochastic optical reconstruction microscopy (STORM) (Figure 5A) (Rust
348 et al., 2006). Unlike host chromatin, whose overall density and compaction scales reproducibly
349 with domain size for active chromatin (Boettiger et al., 2016), viral DNA shows a spatial
350 variability in local density of nearly three orders of magnitude.
351 The greater accessibility and higher variability in local density of viral DNA lend themselves
352 to a possible mechanism by which Pol II becomes enriched. Recent theoretical work has shown
353 that a polymer, like DNA, which has many binding sites in close proximity can induce a particle

354 to revisit the same or adjacent sites repetitively during its exploration of the nucleus (Amitai,
355 2018) (Figure 5B). In such a case, we should be able to see signatures in our spaSPT dataset of
356 Pol II continually revisiting adjacent sites on the viral DNA. To check, we calculated the angle
357 formed by every three consecutive displacements and compiled these angles into a histogram for
358 all particles strictly identified as freely diffusing (see Methods) (Figure 5C) (Izeddin et al.,
359 2014). For particles experiencing ideal Brownian motion, the angular histogram will be isotropic.
360 Anisotropy can arise either by imposing reflective boundaries on the particle, or adding the
361 aforementioned "traps" thereby giving the particle a greater probability of revisiting proximal
362 sites before diffusing away (Amitai, 2018).
363 In uninfected cells, and in infected cells outside of RCs, Pol II displays diffusion that is only
364 mildly anisotropic, consistent with mostly Brownian motion throughout the nucleus. In stark
365 contrast, inside RCs Pol II diffusion is more anisotropic, especially around 180° (Figure 5D). To
366 compare across samples, we computed the likelihood of a backward translocation (180° ± 30°)
367 relative to the likelihood of a forward translocation (0° ± 30°). Analyzed this way, Pol II in an
368 uninfected nucleus has a 1.3-fold greater chance of moving backward after a given translocation
369 than it has of moving forward (Figure 5E). As expected, Pol II outside of RCs in infected cells
370 has a nearly identical value to Pol II in an uninfected cell. Inside of an RC, however, that
371 probability increases to 1.7-fold, showing that this effect is unique to RCs (Figure 5E). In cells
372 treated with Triptolide, we see that when stable binding is inhibited, the effect created by
373 transient binding events is further amplified (Figure 5E). Under this condition, Pol II inside an
374 RC is 2-fold more likely to have a backward displacement after a forward one (Figure 5D),
375 which helps explain the dramatic retention of Pol II inside RCs, even 45 minutes after inhibition
376 of transcription (Figure 3C). Importantly, in uninfected cells where RC annotations have been
377 shuffled *in silico*, no additional anisotropy is observed (Figure S3).
378 These data are most consistent with a model in which Pol II repetitively visits the highly
379 accessible viral genome via multiple weak, transient binding events that result in Pol II rapidly
380 hopping along the DNA. The sharp anisotropy of the molecular exploration within the RC means
381 that a given Pol II molecule that enters an RC is more likely to visit the same site, or sites close
382 in proximity, multiple times before it either finds a stable binding site or diffuses away.
383 The heterogeneous distribution of viral DNA within RCs, and the anisotropic way Pol II
384 explores RCs, is also borne out in the distribution of Pol II molecules. We performed 3D
385 photoactivated localization microscopy (3D PALM) on cells, using adaptive optics for precise
386 3D localization of individual Pol II molecules (Betzig et al., 2006; Izeddin et al., 2012). Similar
387 to the viral DNA, PALM renderings of infected nuclei revealed a heterogeneous Pol II
388 distribution within RCs (Figure 5G). For a more quantitative determination of Pol II clustering,
389 we used Ripley's L-function, a measure of how a spatial point pattern deviates from randomness
390 (Figure 5H) (Nicovich et al., 2017). Here, a value greater than zero indicates a concentration of
391 points higher than predicted for complete randomness at that given radius. For very small radii, a
392 high L(r)-r value is likely due to blinking and other photo-physical artifacts (Annibale et al.,
393 2011). However, our measurements of Ripley's L-function remains well above zero and
394 increases for all radii between 0 and 1000 nanometers, suggesting that Pol II forms hubs within
395 RCs and that this clustering occurs at multiple length scales. This is consistent with other recent
396 studies of Pol II in uninfected cells (Boehning et al., 2018), and in contrast to a structural protein
397 like the CCCTC-binding factor (CTCF), whose L(r)-r curve shows clusters of a single
398 characteristic size (Hansen et al., 2017).

399 **Nonspecific interactions with viral DNA license recruitment of other proteins**

400 Seeing that Pol II is recruited to RCs via transient and nonspecific binding to the viral
401 genome made us wonder whether this effect was specific to Pol II, or whether DNA accessibility
402 can generally drive the recruitment of DNA-binding proteins to RCs. Certainly, many other
403 DNA-binding proteins are recruited to RCs (Dembowski and DeLuca, 2015; Taylor and Knipe,
404 2004). To assess whether nonspecific DNA binding could be responsible for accumulation of
405 other proteins within RCs, we looked at enrichment of the tetracycline repressor (TetR). TetR is
406 a sequence-specific transcription factor found in bacteria that binds with high affinity to the 19
407 bp *tetO* sequence, which is absent in both human and HSV1 genomes (Bolintineanu et al., 2014).
408 Thus, we reasoned that if nonspecific DNA association is the mechanism driving recruitment to
409 the RC, TetR should also be recruited to the RC.
410 We transiently transfected TetR-GFP into the HaloTag-Pol II cell line, then infected them
411 with HSV1 the following day. TetR-GFP, lacking a nuclear localization signal (NLS),
412 ubiquitously occupies both the nucleus and cytoplasm. As predicted by our model, GFP signal
413 was enriched inside of RCs (Figure 6). Pixel line scans of the matched Pol II and TetR channels
414 show that the level of enrichment is modest (~25% over background for TetR, compared with
415 ~200% for Pol II), but the two signals showed a high Spearman correlation ($r > 0.77$). A
416 fluorescent protein with only an NLS showed no enrichment at RCs in infected cells (Figure S8).
417 Thus, even a sequence-specific transcription factor with no cognate binding sites in the viral
418 genome can be recruited to RCs based on its modest affinity for nonspecific DNA sequences.
419 These data suggest a model in which viral Pol II recruitment consists of transient, nonspecific
420 binding/scanning events of the highly exposed viral genome (Figure 7A). A DNA-binding
421 protein exploring the nucleus (uninfected, or infected but outside of RCs) may encounter some
422 occasions for nonspecific interaction with duplex DNA, but because of the condensed nature of
423 the host chromatin, these binding/scanning events are necessarily short (Figure 7B). In addition,
424 it may take a protein many thousands of these transient binding events to finally reach a high-
425 affinity site (Normanno et al., 2015). Within RCs, multiple copies of the highly accessible HSV1
426 genome are present, nonspecific events happen more frequently, with fewer and shorter 3D
427 excursions between DNA contacts (Figure 7C), leading to redundant exploration of the RC and
428 local accumulations of protein. This enrichment becomes even more skewed when aided by a
429 high density of other interactors—for example when transcription is active on the viral DNA,
430 and thus the both specific and general transcription factors are enriched via the same mechanism.
431 Out data strongly indicate, though, that host Pol II accumulation at HSV1 RCs is not dependent
432 on active transcription but instead is largely driven by transient, nonspecific protein-DNA
433 interactions resulting from the high accessibility of the viral DNA.

434 Discussion

435 Multiple routes to create high local concentrations

436 Here we have demonstrated that Herpes Simplex Virus type 1 accumulates Pol II in
437 replication compartments through a novel mechanism: its unusually accessible DNA genome
438 provides many potential nonspecific binding sites, which causes a net accumulation of Pol II,
439 acting as a molecular sink even in the absence of transcription. Such a mechanism for locally
440 concentrating proteins is revealing, as it neither requires the formation of a stable
441 macromolecular structure nor produces any behaviors at the single-molecule level suggesting a
442 separate liquid phase. It is particularly striking because, from the macroscopic view, Pol II
443 recruitment to RCs appears to share many of the behaviors commonly attributed to liquid-liquid

444 phase separation—enrichment of proteins that have high intrinsic disorder, spherical, dynamic
445 structures that undergo fusion, and a change in refractive index—and yet RCs are clearly a
446 distinct class of membraneless compartments.
447 Given the high prevalence of IDRs in the viral proteome, it is likely that they have crucial
448 functions in other aspects of the viral lifecycle, such as the assembly of the capsid or packaging
449 of tegument proteins prior to envelopment. It still remains a possibility that these IDRs form
450 some phase-like system inside of RCs. Crucially, our data demonstrate that, even if this is the
451 case, it does not contribute to the enrichment or entrapment of Pol II. Our results prompt the
452 need for a better characterization of *bona fide* phase separation, with a focus on its functional
453 consequences *in vivo*. These data underscore the importance of rigorously dissecting the diverse
454 mechanisms driving subcellular compartment formation, and suggest that caution should be
455 exercised before immediately assigning LLPS as the primary assembly mechanism or
456 interpreting the functional role of a phase-separated system solely based on macroscopic
457 behaviors.
458 We emphasize that this is certainly not the only means by which herpesviruses interact with
459 Pol II; many other studies have carefully documented the roles of both host and viral proteins in
460 recruiting Pol II to transcribe viral genes (Davis et al., 2015; Zhou and Knipe, 2002). What
461 makes the mechanism proposed above so appealing is that it applies across multiple cellular
462 processes; not just transcription. During its lifecycle, the virus must also utilize other cellular
463 factors such as the DNA replication, repair, and recombination machinery (Dembowski and
464 DeLuca, 2015; Muylaert and Elias, 2007; Taylor and Knipe, 2004). By utilizing nonspecific
465 binding events as a means of attracting DNA-binding proteins and their cofactors, the virus has
466 shifted the equilibrium in those locations, thereby enhancing the probability of regulatory factors
467 binding at specific, functional sites. As a consequence, assembly of typically inefficient multi-
468 protein complexes like the transcription pre-initiation complex (Darzacq et al., 2007), could
469 become more favorable inside of RCs. We speculate that nonspecific protein-DNA interactions
470 could be a general mechanism used by many other viruses. We also note that many RNA-binding
471 proteins have been reported to undergo apparent LLPS (Courchaine et al., 2016) and believe it
472 will be interesting to explore if RNA-binding proteins share a similar mechanism to what we
473 describe here.

474 **Nonspecific binding events represent an important part of nuclear exploration**

475 Our data also reveal a previously underappreciated aspect of how a DNA binding protein
476 finds its target DNA within the nucleus. It has long been recognized that nonspecific binding to
477 DNA could greatly accelerate the target search process by allowing for sliding in 1D along the
478 DNA, thereby reducing the search space and allowing for faster-than-diffusion association
479 kinetics (Berg et al., 1981). This is the case in bacterial systems where DNA is generally
480 accessible to binding. A number of theoretical studies have addressed various aspects of the
481 problem in eukaryotic systems, where TFs compete with nucleosomes for access to DNA
482 (Mirny, 2010). In these cases, the DNA polymer is treated as a surface of variable binding
483 energies on which a transcription factor may slide—if there are no nucleosomes to impede its
484 diffusion (Mirny et al., 2009). *In vivo* experiments using sequence-specific eukaryotic
485 transcription factors find that, for the cases studied, a given factor will spend approximately half
486 its search time undergoing 3D diffusion, and the other half bound nonspecifically, presumably
487 scanning in 1D (Chen et al., 2014; Hansen et al., 2017; Normanno et al., 2015).
488 The data we present here offer a new perspective on the importance of nonspecific and low-
489 affinity binding, and competition for nucleosomes inside the nucleus. When the virus begins

replicating, we measured the newly synthesized DNA to be ~130 times more accessible to DNA-binding proteins than the surrounding host chromatin (Table S3). Not only is there simply more DNA available to bind in the absence of nucleosomes, but the distance that a protein can scan in 1D is greatly increased due to the lack of impeding nucleosomes. Pol II is not a canonical DNA-binding protein, and no systematic study has been undertaken to measure its binding affinities against with different substrates. Still, having evolved to be an enzyme that must transcribe highly diverse DNA sequences suggests that its affinity for DNA outside of an assembled PIC may be relatively high. A recent study which explicitly modeled nonspecific DNA binding in the context of 3D genome organization finds that the most effective regime for recruiting a DNA binding protein is exactly what the virus appears to have settled on—that is a region of low overall DNA density that is free of nucleosomes recruiting a protein with high nonspecific affinity (Cortini and Filion, 2018).

The virus' strategy may be shared by the host in facilitating enhancer-promoter contacts. Both promoter and enhancer elements are identifiable by their increased DNA accessibility. While some recent reports have suggested that enhancers may phase separate as a mechanism of activating transcription (Cho et al., 2018; Hnisz et al., 2017; Sabari et al., 2018), the data presented above suggest that the mechanisms that keep a cluster of enhancers and promoters accessible to DNA-binding proteins may facilitate the accumulation of Pol II and other PIC components, without the need for invoking LLPS.

Mechanism of Pol II recruitment may explain robust transcription of late genes

An unresolved question in the study of herpesviruses is how genes with seemingly weak promoter elements can sustain such robust transcription, especially in the case of late gene promoters which often contain little more than a TATA box and Initiator elements (Rajčáni et al., 2004). How are these transcripts so highly expressed off of such weak promoters? While it is clear that other regulatory components also play a role in regulation of late genes (Davis et al., 2015; Lester and DeLuca, 2011; Li et al., 2018), our data may help shed light on how the virus robustly transcribes them after replication onset. After replication, when there are many copies of the viral genome present in a single RC, the compartmentalization of Pol II (and the other general transcription factors) mediated through nonspecific binding to the viral DNA also favors assembly of PICs at otherwise weak late gene promoters. In this way, the virus can conserve precious sequence space in its genome to encode other important features, and rely on fundamental mechanisms of nuclear exploration for Pol II, and other components of the transcription machinery, to provide sufficient gene expression for these late genes.

524 **Author Contributions**
525 Conceptualization, D.T.M., X.D., and R.T.; Methodology D.T.M., A.S.H., H.M-N., S.T.,
526 X.D., and R.T.; Investigation, D.T.M., Y.H., K.K.U., and C.D-D; Software, D.T.M., A.S.H.,
527 H.M-N., S.T., and A.B.H; Writing – Original Draft, D.T.M; Writing – Review & Editing,
528 D.T.M., A.S.H., H.M-N., S.T., A.B.H, C.D-D, X.D., and R.T.; Funding Acquisition, X.D., and
529 R.T; Resources, C.D-D.; Supervision, D.T.M, X.D., and R.T.

530 **Acknowledgments**
531 We would like to thank James Goodrich, Jennifer Kugel, and Robert Abrisch for providing
532 the HSV1 strain KOS that began this project, and for helpful discussions. Thank you also to Neal
533 DeLuca for the generous gift of the UL2/50 HSV1 strain. Thank you to Luke Lavis for
534 generously providing all of the Janelia Fluor dyes that enabled these experiments. Thank you to
535 Ana Robles and Astou Tangara for their tireless work keeping the microscopes in working order.
536 Thank you to all of the individuals who provided reagents, comments, and critical insight for this
537 manuscript, including Shasha Chong, Thomas Graham, Britt Glaunsinger, Ella Hartenian,
538 Matthew Parker, and the Tjian and Darzacq Lab members. This work was supported by NIH
539 grants UO1-EB021236 and U54-DK107980 (XD), the California Institute of Regenerative
540 Medicine grant LA1-08013 (XD), by the Howard Hughes Medical Institute (003061, RT).
541 Portions of this work were performed on shared instrumentation at the CRL Molecular Imaging
542 Center, supported by The Gordon and Betty Moore Foundation. We would like to thank Holly
543 Aaron and Jen-Yi Lee for their assistance. DNA sequencing in this work used the Vincent J
544 Coates Genomics Sequencing Laboratory at UC Berkeley, supported by NIH 669 S10
545 Instrumentation Grants S10RR029668 and S10RR027303.

546 **Figure Legends**
547 **Figure 1. Pol II recruitment to Replication Compartments exhibit hallmarks of liquid-**
548 **liquid demixing A)** Representative matched images of HaloTag-Pol II labeled with JF_{505} and
549 Spatial Light Interference Microscopy to measure phase shifts for an uninfected cell, and for a
550 cell 5 hpi. Arrows highlight examples of corresponding regions in the two images where an RC
551 shows a significantly different phase value compared with the surrounding nucleoplasm. **B)**
552 Time-lapse images from two cells ("Cell 1" and "Cell 2"). Zoom in shows RCs fusing beginning
553 at t = 204 min and t = 220 min, respectively. HaloTag-Pol II U2OS cells were labeled with JF_{549}
554 and infected, then imaged every 120 seconds beginning 3 hpi. See also Movies S1 and S2. **C)** A
555 histogram of the aspect ratios (max diameter / min diameter) of RCs for 817 individual RCs from
556 134 cells, 3 to 6 hpi. The dotted line marks the median value of 1.18. Red ellipses provided a
557 guide to the eye for different aspect ratios. **D)** IUPred scores for three viral proteins (UL49, RL2,
558 UL54) as a function of residue position. Dashed line indicates an IUPred score of 0.5. Green
559 boxes are predicted to be IDRs. **E)** The fraction of each protein in the viral proteome that is
560 unstructured, separated by kinetic class. Immediate early (IE) and tegument proteins are as
561 enriched in IDRs as a curated list of proteins containing IDRs known to drive phase separation
562 (Cited IDRs). The proteins plotted in panel D are marked with a red circle. **F)** Fluorescence
563 Recovery After Photobleaching (FRAP) curves of Pol II in RCs from 3-4 hpi, 4-5 hpi, and 5-6
564 hpi (n = 24, 33, and 33), compared with uninfected cells (n = 31). Curves represent the mean
565 flanked by SEM. **G)** Representative images from cell lines expressing JF_{549}-labeled HaloTag-
566 RPB1 labeled with JF_{549} with a C-terminal domain containing different numbers of heptad

567 repeats. **H)** Matched fluorescence images of JF_{549}-labeled Pol II and DAPI. Cells were infected
568 with HSV1 for 5 hours, then added 1,6-hexanediol to a final concentration of 10%, and fixed 1, 5
569 and 10 minutes after treatment. All scale bars are 10 µm.
570
571 **Figure 2. spaSPT of Pol II in infected cells shows no change in diffusion but an increase**
572 **in binding. A)** Example frames from a spaSPT movie, overlaid with the results from localization
573 and tracking. Scale bar is 1 µm. **B)** Masks to identify the nuclear boundary (black line) and RCs
574 (green regions) are generated with one color channel (JF_{549}), and these annotations are applied to
575 trajectories from the other color channel (PA-JF_{646}). **C)** Depiction of two-state model where Pol
576 II can either be freely diffusing, or DNA-bound, each with a characteristic rate constant. **D)** Jump
577 length distributions between consecutive frames of spaSPT trajectories. Histograms pooled from
578 uninfected cells (n = 27), or HSV1 infected cells between 4 and 6 hpi (n = 96). Each distribution
579 is fit with a 2-state model. **E)** Mean apparent diffusion coefficient derived from the 2-state fit in
580 (D). Error bars are the standard deviation of the mean, calculated from 100 iterations of
581 randomly subsampling 15 cells without replacement and fitting with the model. **F)** Fluorescence
582 Loss In Photobleaching (FLIP) curves comparing the rate of fluorescence loss after
583 photobleaching JF_{549}-labeled Pol II in uninfected cells and HSV1 infected cells. A 1 µm bleach
584 spot is placed inside an RC (red crosshairs) and bleached between every frame. The loss of
585 fluorescence is measured from another RC (black crosshairs). **G)** Cumulative Distribution
586 Function (CDF) of the mean flanked by the SEM for jump lengths of molecules entering (left) or
587 exiting (right) RCs. Distribution for HSV1 infected cells is compared to the distribution of
588 molecules entering/exiting compartments that have been randomly shuffled around the nucleus
589 *in silico*. **H)** Mean fraction of bound molecules derived from the 2-state fit in (D). Error bars are
590 the standard deviation of the mean, calculated from 100 iterations of randomly subsampling 15
591 cells without replacement and fitting with the model. See also Figures S2, S3A-D, and S4.
592
593 **Figure 3. Pol II recruitment to RCs occurs independent of active transcription. A)**
594 Schematic of Pol II-mediated transcription inhibition. Triptolide (TRP) prevents stable Pol II
595 engagement with the assembled pre-initiation complex. Flavopiridol (FLV) inhibits engaged Pol
596 II from elongating past ~50 bp. B) Schematic of experiment regimen for imaging infected cells
597 after transcription inhibition. Cells are infected at time 0. At 4 hpi, cells are treated with
598 transcription inhibitors Flavopiridol (FLV) or Triptolide (TRP) and fixed after 15, 30, or 45
599 minutes. For live cell imaging, cells are treated with drug at 4 hpi, and after 30 minutes, they are
600 mounted on the microscope and imaged directly. C) Representative images of JF_{549}-labeled
601 HaloTag-Pol II and DAPI after 45 minutes of Triptolide or Flavopiridol treatment. All scale bars
602 are 10 µm. D) Mean fraction bound measured from spaSPT of HaloTag-Pol II, after either
603 Flavopiridol or Triptolide treatment. Error bars are the standard deviation of the mean, calculated
604 from 100 iterations of randomly subsampling 15 cells without replacement and fitting with the
605 model. E) FRAP recovery curves of Pol II with (hashed) and without (solid) Triptolide treatment,
606 for uninfected cells (N = 31, 9 respectively) and cells infected with HSV1, 5hpi (N = 32, 12
607 respectively). Also see Figure S5.
608
609 **Figure 4. ATAC-seq reveals HSV1 DNA is much more accessible than chromatin. A)**
610 Schematic representation of where Oligopaint probes target within the viral genome for DNA
611 Fluorescence In Situ Hybridization. AlexaFluor 647-labeled probes target a 10,016 bp region in
612 the middle of the Unique Long (UL) arm. AlexaFluor 555-labeled probes target a 7703 bp region

613 in the middle of the Unique Short (US) arm. **B)** Representative images of DNA FISH on cells
614 infected in the presence of the replication inhibitor phosphonoacetic acid (PAA, left) and 4 hpi
615 (right). Pixel intensity values are the same for the two images. Scale bars are 10 μm. **C)**
616 Quantification of fluorescence intensity of DNA FISH signal in RCs at increasing times after
617 infection. Data are normalized to the median intensity value of cells infected in the presence of
618 the replication inhibitor PAA. Medians are indicated by a solid line (PAA = 1, 3 hpi = 0.83, 4 hpi
619 = 4.77, 5 hpi = 31.13, 6 hpi = 46.95). Also see Figure S5 **D)** Mean fraction bound extracted from
620 2-state model of PA-JF_{646}-labeled HaloTag-Pol II, comparing HSV1 infected cells between 4 and
621 6 hpi to cells infected in the presence of PAA. Error bars are the standard deviation of the mean,
622 calculated from 100 iterations of randomly subsampling 15 cells without replacement and fitting
623 with the model. **E)** Fragment length distribution of ATAC-seq data for cells 4 hpi. Reads
624 mapping to the human genome are in gray, and reads mapping to the HSV1 genome are in green,
625 and data are normalized to the total number of reads mapping to each organism. Lengths
626 corresponding to intra-nucleosomal DNA (50–100 bp) and mononucleosomal DNA (180-250 bp)
627 are marked as a reference. **F)** ATAC-seq read density for all fragment lengths plotted across
628 HSV1 genomic coordinates for uninfected cells, and for 2, 4, and 6 hpi. **G)** ATAC-seq analysis
629 of intra-nucleosomal DNA (50–100 bp) and mononucleosomal DNA (180-250 bp). Global
630 analysis of all human Pol II-transcribed genes, centered at the transcription start site (TSS) at
631 different times after infection. **H)** The same analysis as in (G), but centered at the TSS of HSV1
632 genes. Also see Figures S6 and S7.
633
634 **Figure 5. DNA-binding alters Pol II exploration of RCs. A)** Representative STORM
635 image of an HSV1 infected cell in the presence of EdU to allow labeling with AlexaFluor 647
636 and matched diffraction-limited images and STORM reconstruction, rendered with 20 nm by 20
637 nm pixels. Zoom-in shows one RC, and the heatmap shows the number of fluorophore
638 localizations occurred in each rendered pixel. **B)** Schematic of Pol II entering an RC and
639 randomly sampling the viral DNA, sometimes revisiting the same, or closely adjacent, sites
640 before diffusing away. **C)** Example spaSPT trace, with each set of three localizations (n, n+1,
641 n+2) forming a measurable angle (θ_n…). **D)** Angular distribution histograms extracted from
642 diffusing HaloTag-Pol II molecules in uninfected cells, and HSV1 infected cells 4-6 hpi, inside
643 and outside of RCs. Shaded regions highlight the angles used to calculate the relative probability
644 of moving backward compared to forward in (E). **E)** Quantification of the relative probability of
645 moving backward compared to forward (180° ± 30° / 0° ± 30°). Error bars are the standard
646 deviation of the mean, calculated from 100 iterations of randomly subsampling 15 cells without
647 replacement. **F)** Same as in (D), except that cells were treated with Triptolide at least 30 minutes
648 prior to imaging. Quantification of this data is also show in (E). **G)** Representative PALM image
649 of PA-JF_{646}-labeled HaloTag-Pol II, rendered with a pixel side of 20 nm by 20 nm. Infected cells
650 were identified by immunofluorescence against the HSV1 protein ICP4. Heatmap corresponds to
651 the number of detections per rendered pixel. Dotted red lines mark the outlines of RCs, as
652 identified by the immunofluorescence image. **H)** L-modified Ripley Curve (L(r)-r) for HaloTag-
653 Pol II inside of RCs in cells 5 hpi (n = 13 cells). Graph shows the mean flanked by the SEM. All
654 scale bars are 10 μm. Also see Figure S3E and S3F.
655
656 **Figure 6. Nonspecific DNA binding drives accumulation of other factors in RCs. A)**
657 Representative images of HaloTag-Pol II cells transiently transfected with TetR-GFP prior to
658 infection with HSV1. **B)** Pixel line scans of images in (A). Red arrows in (A) give the direction

659 of the x-axis. Left axis is the intensity of TetR-GFP fluorescence, right axis is the intensity of
660 JF_{549}-labeled HaloTag-Pol II fluorescence. Spearman's correlation was used to measure the
661 covariation in the two channels across the line. All scale bars are 10 μm. Also see Figure S8.
662
663 **Figure 7. Model for Pol II exploration of RCs. A)** A Pol II molecule encounters the
664 accessible viral DNA multiple times along one potential route to eventually bind at a promoter.
665 3D diffusion through the RC is interrupted by binding interactions with the viral DNA (gray
666 circles). These binding interactions may be very transient in nature, and may involve direct
667 interaction with the viral DNA, 1D scanning along the DNA, or transient interactions with other
668 DNA-associated proteins. **B)** Hypothetical comparison of nuclear exploration outside RCs as a
669 function of time and binding energy. A DNA-binding protein in the chromatinized nucleus will
670 encounter naked DNA sporadically, making multiple low-affinity interactions before eventually
671 finding a high affinity site. **C)** Inside an RC, the high DNA accessibility might shorten the length
672 of 3D excursions before a DNA-binding protein encounters another region of viral DNA in a low
673 affinity, nonspecific interaction. This, in turn, may reduce the distance a molecule might diffuse
674 before its next binding event, and increases both the chances of that molecule remaining in close
675 proximity and the chances that it will find a high binding energy interaction.

676 **Supplementary Figure Legends**
677 **Figure S1 – RCs remain round, particularly at early times in infection.** Related to **Figure**
678 **1**. **A)** Histograms of the aspect ratios (Maximum diameter / minimum diameter) for RCs from
679 cells at 3-4 hpi (n = 219), 4-5 hpi (n = 302), and 5-6 hpi (n = 296). **B)** Aspect ratio of every
680 measured RC, as a function of its size measured in μm^2. Dot colors correspond to the data sets in
681 (A).
682
683 **Figure S2 – Dendra2 photoconversion shows Pol II exchanges with nucleoplasm.**
684 Related to **Figure 2**. Cells stable expressing Dendra2-Pol II were infected with HSV1.
685 Fluorescence was monitored in both the green channel (pre-conversion), and red channel (post-
686 conversion). A 1μm spot of 405nm light was used to convert one RC from green to red,
687 alternating between photoconversion and frame acquisition. All scale bars are 10 μm.
688
689 **Figure S3 – Comparison of *bona fide* RCs with RCs generated *in silico*.** Related to
690 **Figure 2**. **A)** Example workflow for uninfected cells, where either just the nucleus was masked
691 (left), or the nucleus was masked and RC-sized annotations were randomly placed inside the
692 nucleus (right). **B)** Example workflow for HSV1 infected cells, where both the correct
693 annotations based on the widefield image and randomly shuffled RCs were generated for all
694 measured cells. **C)** Spot-On measurements of trajectories after inside/outside classification in
695 uninfected cells. *In silico* shuffling of RC positions has very little effect on either the measured
696 apparent diffusion coefficient or the fraction bound. Error bars are the standard deviation of the
697 mean, calculated from 100 iterations of randomly subsampling 15 cells without replacement and
698 fitting with the model. **D)** Similar to (C), but for infected cells. Real RCs show an increase in
699 fraction bound, whereas *in silico* shuffled compartments show no difference with trajectories
700 outside RCs. **E)** Angular distributions of Pol II trajectories in the regions marked in (A)
701 Fold(180/0) is the mean plus/minus the standard deviation, calculated from 100 iterations of
702 randomly subsampling 15 cells without replacement and fitting with the model. **F)** Angular
703 distributions of Poll II trajectories in the regions marked in (B). Fold(180/0) is the mean

704 plus/minus the standard deviation, calculated from 100 iterations of randomly subsampling 15
705 cells without replacement and fitting with the model. All scale bars are 10µm.
706
707 **Figure S4 – Diffusion coefficient of Bound population is consistent with chromatin**
708 **binding.** Related to **Figure 2**. Mean diffusion coefficient of the Bound population determined
709 through 2-state model fitting for uninfected cells, and for cells at different times post infection,
710 both inside and outside of RCs. In all data sets, the calculated diffusion coefficient is well below
711 the upper bound set for the fitting, consistent with diffusion coefficients of chromatin (Hansen et
712 al., 2018). Error bars are the standard deviation of the mean, calculated from 100 iterations of
713 randomly subsampling 15 cells without replacement and fitting with the model.
714
715 **Figure S5 – Transcription inhibition does not remove Pol II from RCs.** Related to **Figure**
716 **3**. **A)** Representative images of U2OS cells, 4 hpi, either untreated or treated with the
717 transcription inhibitors flavopiridol or triptolide. FISH probes against the intron to the HSV1
718 gene RL2 mark ongoing transcription, while immunofluorescence against the viral protein ICP8
719 marks infected cells by their RCs. All images within a color channel have been matched to have
720 the same minimum and maximum pixel values. All scale bars are 10µm. **B)** Quantitation of
721 transcription inhibition from (A). The FISH intensity in a 1µm z-section is compared in RCs
722 from untreated cells (n = 170 RCs) to those treated for 15, 30, or 45 minutes with TRP(n = 192,
723 171, 191 RCs, respectively) and FLV(n = 158, 238, 153 RCs, respectively). Error bars represent
724 standard error of the mean. **C)** Quantitation of Pol II recruitment to RCs from conditions in (A).
725 The Pol II fluorescence intensity in a 1µm z-section is compared in RCs from untreated cells (n =
726 247 RCs) to those treated for 15, 30, or 45 minutes with TRP(n = 276, 206, 270 RCs,
727 respectively) and FLV(n = 292, 246, 325 RCs, respectively). Error bars represent standard error
728 of the mean.
729
730 **Figure S6 – Quantification of DNA content in HSV1 RCs.** Related to **Figure 4. A)** Dot
731 plot showing the individual RC values from Figure 4C; normalized to the median of cells
732 infected in the presence of PAA. Medians are indicated by a solid line (PAA = 1, 3 hpi = 0.83, 4
733 hpi = 4.77, 5 hpi = 31.13, 6 hpi = 46.95). **B)** Genome content of individual RCs in (A), plotted as
734 a function of their area. Spot color corresponds to the times post infection as in (A). Line is a
735 lease squares quadratic fit to all data points (R^2 = 0.83).
736
737 **Figure S7 – HSV1 genome appears nucleosome free at all times tested.** Fragment length
738 distributions of all conditions tested after HSV1 infection, for two individual replicates as well as
739 for the pooled data. The green line indicates the lengths of fragments mapping to the viral
740 genome, the gray line indicates lengths of fragments mapping to the human genome. All data are
741 normalized to the total number of mapped reads to the respective genome, per condition.
742
743 **Figure S8 – YFP-NLS does not colocalize with RCs. A)** Representative images from cells
744 transfected with YFP-NLS and then infected with HSV1. YFP-NLS forms occasional puncta in
745 the nucleus, but these do not overlap with RCs, as marked by Pol II. **B)** Pixel line scans of
746 images in (A). Red arrows in (A) give the direction of the x-axis. Left axis is the intensity of
747 YFP-NLS fluorescence, right axis is the intensity of JF_{549}-labeled HaloTag-Pol II fluorescence.
748 Spearman's correlation was used to measure the covariation in the two channels across the line.
749 All scale bars are 10 µm.

750
751 **Table S1 – List of putative IDRs in the HSV1 genome identified by IUPred.** Each protein
752 listed was analyzed as described in the Methods section, and regions with an IUPred score of
753 greater than 0.55 were recorded.
754
755 **Table S2 – List of proteins reported to undergo phase separation.** Gene name, organism
756 of origin, size, and the fraction of the protein that scores as an IDR according to the analysis
757 described in the Methods section. References and the citation within and provided.
758
759 **Table S3 – Quantitative measurements of HSV1 DNA inside of RCs.** Using the values
760 obtained through DNA FISH and ATAC-seq, we can make estimates of the copy number,
761 concentrations, and relative enrichment of the viral DNA compared to the host. All values are
762 calculated based on measurements of cells 6 hpi.
763
764 **Movie S1 and S2 – Time lapse movies of HaloTag-Pol II after HSV1 infection.** Cells
765 were identified 3 hpi, and followed until they moved out of the focal plane.

766 **Experimental Procedures**

767 **Tissue Culture**

768 Human U2OS cells (female, 15 yr old, osteosarcoma) were cultured at 37°C and 5% CO2 in
769 1 g/L glucose DMEM supplemented with 10% Fetal Bovine Serum and 10 U/mL Penicillin-
770 Streptomycin, and we subcultivated at a ratio of 1:3 – 1:6 every two to four days. Stable cell
771 lines expressing the exogenous gene product α-amanitin resistant HaloTag-RPB1(N792D) or
772 Dendra2-RPB1(N792D) were generated using Fugene 6 following the manufacturer's protocol,
773 and selection with 2 μg/mL α-amanitin. Stable colonies were pooled and maintained under
774 selection with 1 μg/mL α-amanitin to ensure complete replacement of the endogenous RPB1
775 pool, as described previously (Boehning et al., 2018; Cisse et al., 2013).
776 Vero cells, were cultured for the growth and propagation of HSV1. Vero cells were cultured
777 at 37°C and 5% CO2 in 4.5 g/L glucose DMEM supplemented with 10% Fetal Bovine Serum
778 and 10 U/mL Penicillin-Streptomycin. Cells were subcultivated at a ratio of 1:3 – 1:8 every two
779 to four days.
780 HSV1 Strain KOS was a generous gift from James Goodrich and Jennifer Kugel (Abrisch et
781 al., 2015). UL2/50 was a generous gift from Neal DeLuca (Dembowski and DeLuca, 2015). All
782 virus strains were propagated in Vero cells as previously described (Blaho et al., 2005). Briefly,
783 cells were infected by incubation at an MOI ~ 0.01 in Medium 199 (Thermo) for one hour. 36-48
784 hpi, cells were harvested by freeze-thawing, pelleted, and sonicated briefly, and then centrifuged
785 to clear large cellular debris. Because we were interested in the early events in infection,
786 approximate titers were first determined by plaque formation assay in Vero cells (Blaho et al.,
787 2005). More accurate MOI were determined by infecting U2OS cells plated on coverslips with
788 the same protocol as would be using for imaging experiments. Cells were washed once with
789 PBS, and then 100 μL of complete medium containing 1:10 – 1:10^5 dilutions of harvested virus
790 were added dropwise onto the coverslip to form a single meniscus on the coverslip. Infection was
791 allowed to proceed for 15 minutes at 37 °C. Samples were then washed once with PBS and
792 returned to culturing medium and incubated for 8 hours before fixation. To measure the MOI,
793 immunofluorescence for the expression of ICP4 using an anti-ICP4 primary antibody (Abcam),

794 and counting the number of infected versus uninfected cells. MOI was then calculated, assuming
795 a Poisson distribution of infection events, as $P(k_{inf}) = \frac{MOI^{k_{inf}} e^{-MOI}}{k_{inf}!}$, where k_{inf} is the number of
796 infection events per cell. When counting the uninfected cells, this simplifies to
797 $MOI = -\ln(f_{uninfected})$. All experiments were performed from the same initial viral stock,
798 with care taken so that each experiment was done with virus experiencing the same total number
799 of freeze/thaw cycles to ensure as much consistency as possible.

800 **Live cell imaging**

801 Cells were plated on plasma-cleaned 25 mm circular No. 1.5H cover glasses (Marienfeld
802 High-Precision 0117650) and allowed to adhere overnight. For experiment using Halo-RPB1,
803 cells were incubated with 50 – 500 nM fluorescent dye (e.g. JF_{549}) conjugated with the HaloTag
804 ligand for 15 minutes in complete medium. Cells were washed once with PBS, and the media
805 replaced with imaging media (Fluorobrite media (Invitrogen) supplemented with 10% FBS and
806 10 U/mL Penicillin-Streptomycin). Prior to imaging, coverslips were mounted in an Attofluor
807 Cell Chamber filled with 1 mL of imaging medium. Cells were maintained at 37 °C and 5 %
808 CO2 for the duration of the experiment. For long term time course imaging experiments, cells
809 were plated in 35mm No. 1.5 glass-bottomed imaging dishes (MatTek), infected with HSV1 at
810 an MOI of ~1, and labeled with $JF_{549,}$ and finally the media exchanged for imaging media before
811 placing in a pre-warmed Biostation (Nikon). At 3 hours post infection, infected cells were
812 identified and imaged were taken every 30 seconds for 5 hours. For phase images, cells were
813 plated and labeled as above, and imaged on a custom-built widefield microscope with a SLIM
814 optics module (PhiOptics) placed in the light path directly before the camera.

815 **IUPred disorder prediction**

816 Disorder predictions were preformed using a custom built python script to implement the
817 IUPred intrinsic disorder prediction program (Dosztanyi et al., 2005; Dosztányi et al., 2005).
818 Specific protein sequences were placed in a table and this was fed into the script. All protein
819 sequences were downloaded from the reference organism at uniport.org. The resulting traces
820 were smoothed by a rolling mean of 8 residues to remove noise and prevent single low-energy
821 residues from splitting single large IDRs into multiple apparent IDRs. Contiguous substrings of
822 residues with centered-mean IUPred disorder likelihood greater than 0.55 were annotated as
823 "disordered regions" (Fig. 1E), and those contiguous regions larger than 10 amino acids were
824 included in the calculation of “fraction IDR”.

825 **Fluorescence Recovery After Photobleaching (FRAP)**

826 FRAP experiments were performed as previously described, with modifications. HaloTag-
827 RPB1 cells labeled with 500 nM JF_{549} were imaged on an inverted Zeiss LSM 710 AxioObserver
828 confocal microscope with an environment chamber to allow incubation at 37°C and 5% CO_2.
829 JF_{549} was excited with a 561 nm laser, and the microscope was controlled with Zeiss Zen
830 software. Images were acquired with a 63x Oil immersion objective with a 3x optical zoom.
831 1200 total frames were acquired at a rate of 250 msec per frame (4 Hz). Between frames 15 and
832 16, an 11-pixel (0.956 µm) circle was bleached, either in the center of a RC, or in a region of the
833 nucleus far from the nuclear periphery or nucleoli.

834 FRAP movies were analyzed as previously described (Hansen et al., 2017). Briefly, the
835 center of the bleach spot was identified manually, and the nuclear periphery segmented using
836 intensity thresholding that decays exponentially to account for photobleaching across the time of
837 acquisition. We measured the intensity in the bleach spot using a circle with a 10 pixel diameter,

838 to make the measurement more robust to cell movement. The normalized FRAP values were
839 calculated by first internally normalizing the signal to the intensity of the whole nucleus to
840 account for photobleaching, then normalizing to the mean value of the spot in the first 15 frames.
841 We corrected for drift by manually updating a drift-correction vector with the stop drift every
842 ~40 frames. FRAP values from individual cells were averaged across replicates to generate a
843 mean recovery curve, and the error displayed is the standard error of the mean.

844 **Fluorescence Loss in Photobleaching (FLIP)**

845 FLIP experiments were performed on the same microscope described above for FRAP.
846 Rather than bleach an 11-pixel spot a single time, in FLIP the spot is bleached with a 561 nm
847 laser (or in the case of Dendra2, photoconverted with a 405 nm laser) between each acquisition
848 frame. Movies were collected for 1000 frames at 250 msec per frame (4 Hz), or 1 frame per
849 second (1 Hz) for Dendra2.

850 FLIP movies were analyzed using the same core Matlab code as the FRAP data, except that
851 fluorescence intensities from another 10-pixel circle were recorded to measure the loss of
852 fluorescence elsewhere in the nucleus. This analysis spot was chosen to be well away from the
853 bleach spot, either at a neighboring RC in infected samples or somewhere else in the
854 nucleoplasm far away from both the nuclear periphery and nucleoli. Instead of internally
855 correcting for photobleaching, photobleaching correction was based on an exponential decay
856 function empirically determined to be at a rate of $e^{-0.09}$ per frame. FLIP data from multiple cells
857 were averaged together to determine the mean and standard error for a given condition.

858 **RNA Fluorescence In Situ Hybridization (FISH) and immunofluorescence (IF)**

859 RNA FISH was used to measure the transcription output for a given RC. To ensure we were
860 measuring nascent transcription, we chose to tile the intronic region of RL2, one of the few
861 HSV1 transcripts with an intron. The 25 oligonucleotide probes were synthesized conjugated
862 with a Cal Fluor 610 dye (Biosearch Technologies). FISH was performed based on the
863 manufacturer's protocol. Briefly, cells were plated on 18 mm No. 1.5 coverslips (Marienfield)
864 and infected. At the desired time point, cells were fixed in 4% Paraformaldehyde diluted in PBS
865 for 10 minutes. After two washes with PBS, coverslips were covered with 70% v/v ethanol and
866 incubated at -20 °C for 1 hour up to 1 week.

867 For hybridizations, coverslips were removed from ethanol and washed in freshly-prepared
868 Wash Buffer A (2 volumes 5x Wash Buffer A, 1 volume formamide, 7 volumes H_2O) (Bioseach
869 Technologies). Hybridization buffer (10% v/v Dextran Sulfate, 300 mM Sodium Chloride, 30
870 mM Sodium Citrate, 400, 10% Formamide v/v, and 12.5 nM pooled fluorescent probes) was
871 prepared freshly before each hybridization. A hybridization chamber was prepared with
872 moistened paper towels laid in a 15cm tissue culture plate. A single sheet of Parafilm was laid
873 over the moistened paper towel. 50 µL of hybridization buffer was pipetted onto the parafilm,
874 and a coverslip inverted into the hybridization buffer. The chamber was sealed with parafilm and
875 placed in a dry 37 °C oven for 4-16 hours. After hybridization, coverslips were placed back into
876 a 12-well plate containing 1 mL Wash Buffer A and incubated twice for 20 minutes in a dry oven
877 at 37 °C, with the second wash containing 300 nM DAPI. In a final wash step, cells were washed
878 in Wash Buffer B (Biosearch Technologies). Coverslips were mounted on glass microscope
879 slides in Vectashield mounting medium (Vector Laboratories) and the edges sealed with clear
880 nail polish (Electron Microscopy Sciences). For experiments with combined
881 immunofluorescence and FISH, primary antibody was added to the hybridization buffer at a
882 concentration of 2 µg/mL. An additional wash step with Wash Buffer A containing 1µg/mL anti-

883 mouse polyclonal antibody conjugated to AlexaFluor 647 was performed before DAPI staining,
884 and incubated at 37°C for 20 minutes.
885 Samples were imaged on a custom built epifluorescence Nikon Eclipse microscope equipped
886 with piezoelectric stage control and EMCCD camera (Andor), as well as custom-built filter sets
887 corresponding to the wavelength of dye used. All samples were imaged the same day after
888 hybridaztion and/or incubation with secondary antibody, and all samples to be quantitatively
889 compared across coverslips were imaged on the same day using exactly the same illumination
890 and acquisition settings to minimize coverslip-to-coverslip variation.

891 **Single Particle Tracking (spaSPT)**

892 Single particle tracking experiments were carried out as previously described (cit), but are
893 described here in brief. After overnight growth, U2OS cells expressing Halo-RPB1 were labeled
894 with 50 nM each of JF_{549} and PA-JF_{646}. Single molecules imaging was performed on a custom-
895 built Nikon Ti microscope fitted with a 100x/NA 1.49 oil-immersion TIRF objective, motorized
896 mirror are to allow HiLo illumination of the sample, Perfect Focus System, and two aligned EM-
897 CCD cameras. Samples were illuminated using 405- nm (140 mW, OBIS coherent), 561-nm (1
898 W, genesis coherent), and 633-nm (1 W, genesis coherent) lasers, which were focused onto the
899 back pupil plane of the objective via fiber and multi-notch dichromatic mirror (405-nm/488-
900 nm/561-nm/633-nm quad-band; Semrock, NF03-405/488/532/635E-25). Excitation intensity and
901 pulse width were controlled through an acousto-optic transmission filter (AOTF nC-VIS-TN, AA
902 Opto-Electronic) triggered using the camera's TTL exposure output signal. Fluorescence
903 emissions were filtered with a single bandpass filter in front of the camera (Semrock 676/37 nm
904 bandpass filter). All of the components of the microscope, camera, and other hardware were
905 controlled through NIS-Elements software (Nikon).
906 For all spaSPT experiments, frames were acquired at a rate of 7.5 msec per frame (7 msec
907 integration time plus 0.447 msec dead time). In order to obtain both the population-level
908 distribution of the molecules for masking and the single trajectories, we used the following
909 illumination scheme: First 100 frames with 561 nm light and continuous illumination were
910 collected; then 20,000 frames with 633 nm light at 1 msec pulses per frame and 0.4 msec pulses
911 of 405 nm light during the camera dead time; then 100 frames with 561 nm light and continuous
912 illumination were collected. 405 nm illumination was optimized to achieve a mean density of ~
913 0.5 localizations per camera frame.

914 **spaSPT data processing**

915 SPT data sets were processed in 4 general steps using a custom-written Matlab (Mathworks):
916 1) Masks for RCs were annotated manually, 2) the masks were corrected for drift throughout the
917 sample acquisition, 3) particles were localized and trajectories constructed, and 4) trajectories
918 were sorted as "inside" compartments or "outside".
919 First, the 100 frames at the beginning and the end of each movie were separately extracted
920 and a maximum-intensity projection used to generate "before" and "after" images of the cell or
921 cells in the field of view. These images would be used to correct for movement of the cell as well
922 as the individual RCs. For each cell, the nucleus was annotated in the "before" image, and then
923 again in the "after" image. We assumed that the cell movement over the ~4 minutes of
924 acquisition was approximately linear, and calculated the drift-corrected nuclear boundary for
925 every frame in the stack of SPT images. The same procedure was applied to each of the
926 replication compartments. Particle localization and tracking were implemented based on an
927 adapted version of the Multiple Target Tracking (MTT) algorithm, available at
928 https://gitlab.com/tjian-darzacq-lab/SPT_LocAndTrack. In the first step, particles were identified

929 with the following input parameters: Window = 9 px; Error Rate = $10^{-6.25}$; Deflation Loops = 0.
930 Following detection, a mask generated from the drift-corrected nuclear boundary was applied to
931 discard any detections not within the nucleus. Trajectories were reconstructed with the following
932 parameters: Dmax = 10 μm^2/sec; Search exponent factor = 1.2; Max number of competitors = 3;
933 Number of gaps allowed = 1.
934 Finally, after trajectories have been reconstructed, they were sorted as "inside" RCs or
935 "outside". To minimize the potential for bias in calling trajectories inside of compartments, we
936 only required a single localization in a trajectory to fall within a compartment for that trajectory
937 to be labeled as "inside". As is discussed in the main text, we tested this sorting strategy for
938 implicit bias by computationally generating mock RCs in uninfected or infected samples (Figure
939 S3). To do this, all of the annotations for RCs from the infected samples (n = 817), as well as the
940 distribution of number of RCs per infected cell, were saved in a separate library. We then took
941 the uninfected cells and, in a similar process as described above, annotated the nuclear boundary
942 and nucleoli. We then randomly sampled from distribution of RCs per cell a number of RCs to
943 place in the nucleus, and then from the library of annotations randomly chose these RCs and
944 placed them in the nucleus by trial-and-error until all of the chosen RCs could be placed in the
945 nucleus without overlapping with each other, a nucleolus, or the nuclear boundary (Figure S3A).
946 The SPT data were then analyzed as above—drift-correction, followed by localization, building
947 of trajectories, and sorting into compartments—using the exact same parameters. We also
948 followed this same procedure of randomly choosing and placing artificial RCs in infected cells,
949 this time avoiding previously annotated RCs instead of nucleoli (Figure S3B).

950 **Two-state kinetic modeling using Spot-On**

951 We employed the Matlab version of Spot-On (available at https://spoton.berkeley.edu) in our
952 analysis, and embedded this code into a custom-written Matlab routine. All data for a given
953 condition were merged, and histograms of displacements were generated for between 1 and 7 Δt.
954 These histograms were fitted to a two-state kinetic model which assumes one immobile
955 population and one freely diffusing population: Localization Error = 45 nm; D_{free} = [0.1 μm^2/sec,
956 5 μm^2/sec]; D_{bound} = [0.001 μm^2/sec, 0.3 μm^2/sec]; Fraction Bound = [0, 1]; UseWeights = 1;
957 UseAllTraj = 0; JumpsToConsider = 4; TimePoints = 7; dZ = 0.700. Trajectory CDF data were
958 fit to a two-state model as first outlined by Mazza and colleagues, and expanded with
959 implementation in Hansen and colleagues.
960 Because of the sparsity of the data we collected, we could not reliably generate single-cell
961 statistics. In order to estimate the variability in the data, we implemented a random subsampling
962 approach where 15 cells from a particular condition were randomly chose and analyzed. The
963 D_{free}, D_{bound}, and Fraction Bound were calculated for all trajectories, for trajectories inside of
964 RCs, and for trajectories outside of RCs. This process was repeated 100 times, and the median
965 values and standard deviations calculated and reported.

966 **Analysis of angular distribution**

967 Angular distribution calculations were performed using a custom written routine in Matlab,
968 implementing a previous version of this analysis (available at
969 https://gitlab.com/anders.sejr.hansen/anisotropy). To analyze the angular distribution of
970 trajectories in different conditions, we started with the list of trajectories generated above,
971 annotated as either "inside" or "outside" of RCs. A trajectory of length N will have N-2 three-
972 localization sets that form an angle, and so we built a matrix consisting of all consecutive three-
973 localization sets. It is crucially important that only diffusing molecules be considered in the
974 analysis, as localization error of bound molecules would skew all of the data to be highly

975 anisotropic. To address this, we used two criteria. First, we only applied a Hidden-Markov
976 Model based trajectory classification approach to classify trajectories as either diffusing or bound
977 (Persson et al., 2013), and kept only the trajectories that were annotated as diffusing. Second, we
978 applied a hard threshold that both translocations (1 to 2, 2 to 3) had to be a minimum of 150 nm,
979 which ensured that we could accurately compute the angle between them. Because a particle may
980 diffuse into or outside of the annotated region, we counted a trajectory as "inside" only if the
981 vertex of the angle occurred within an annotated region.

982 **ATAC-seq**

983 ATAC-seq experiments were performed as previously described (Buenrostro et al., 2013).
984 Briefly, 100,000 U2OS cells stably expressing HaloTag-RPB1 were plated and allowed to grow
985 overnight. The following day, cells were infected as described above, and incubated either in
986 complete medium, or complete medium supplemented with 300 µg/mL phosphonoacetic acid
987 (PAA). Infections were timed such that all cells were harvested at once. All of the infected cell
988 lines were then trypsinized, and 100,000 cells were transferred to separate eppendorff tubes.
989 Cells were briefly centrifuged at 500 xg for 5 minutes at 4°C, and the supernatant discarded.
990 After one wash with ice-cold PBS and another 5 minute spin at 500 xg and 4°C, cells were
991 resuspended directly in tagmentation buffer (25µL 2x Buffer TD, 22.5 µL nuclease free water,
992 2.5µL Tn5 (Illumina)) and incubated for 30 minutes at 37 °C. DNA extraction and amplification
993 with barcodes were performed as previously described, with 10-16 total cycles amplification.
994 Barcoded samples were pooled in equimolar amounts and sequenced using a full flow-cell of an
995 Illumina Hi-Seq 2500 per replicate. Two replicates were performed. Sequenced reads were
996 mapped separately to hg19 genome using Bowtie2 (Langmead and Salzberg, 2012) with the
997 following parameters: --no-unal --local --very-sensitive-local --no-discordant --no-mixed --
998 contain --overlap --dovetail --phred33. Reads were separately mapped to the HSV1 genome,
999 JQ673480, using Bowtie2 with the following parameters: --no-unal --no-discordant --no-mixed -
1000 -contain --overlap --dovetail --phred33. The bam files were converted to bigwig files and
1001 visualized using IGV (Robinson et al., 2011). TSS plots were generated using Deeptools suite
1002 (bamCoverage, computeMatrix, plotHeatmap tools) using UCSC TSS annotations for hg19
1003 genome, and using a highly refined map of the gene starts in HSV1 kindly provided by Lars
1004 Dölken (University of Cambridge, to be published separately).

1005 **Oligopaint on infected cells**

1006 For DNA FISH experiments, custom pools of fluorescently labeled DNA oligos were
1007 generated using previously published protocols (Beliveau et al., 2015; Boettiger et al., 2016).
1008 Briefly, oligo sequences tiling a 10,016 bp region in the Unique Long arm (JQ673480 position
1009 56,985 to 66,999) and a 7703 bp region in the Unique Short arm (JQ673480 position 133,305 to
1010 141,007) were manually curated using oligo BLAST (NCBI) against the HSV1 and human
1011 genomes with the following settings, following guidelines for Tm, GC-content, and length from
1012 previous Oligopaint protocols (Beliveau et al., 2012; Boettiger et al., 2016). Individual oligos
1013 were synthesized and pooled. PCR was used to introduce a common T7 promoter on the 3' end
1014 of the final probe sequence, then the PCR products were gel purified before *in vitro* transcription
1015 to generate ssRNA complimentary to the hybridization sequence. Finally, the entire RNA pool
1016 was reverse transcribed in a single reaction using Maxima RT (Thermo) using either AlexaFluor-
1017 647 or AlexaFluor-555 5'-labeled oligos as the reverse transcription primer. After acid
1018 hydrolysis to remove the RNA, oligos were purified using high binding capacity oligo cleanup
1019 columns (Zymo) and resuspended in TE.

1020 Cells were plated on 18 mm coverslips and infected as described above. Infected was
1021 allowed to progress for between 3 and 8 hours in the presence or absence of phosphonoacetic
1022 acid, then fixed with 4% paraformaldehyde for 15 minutes. Coverslips were washed twice with
1023 PBS, then incubated with 100mM Glycine in PBS for 10 minutes. Samples were permeabilized
1024 for 15 minutes with 0.5% Triton-X100 in PBS, then washed twice with PBS. After
1025 permeabilization, samples were treated with 100 mM HCl for 5 minutes, then washed twice with
1026 PBS. Prior to hybridization, samples were washed twice with 2X SSC (300 mM NaCl, 30 mM
1027 Sodium Citrate), and then incubated at 42 °C for 45 minutes in 2X SSC with 50% v/v
1028 Formamide. Coverslips were inverted onto a slide containing 25 µL hybridization buffer (300
1029 mM NaCl, 30 mM Sodium Citrate, 20% w/v Dextran Sulfate, 50% v/v Formamide, and 75 pmol
1030 of fluorescently-labeled oligos) and sealed with rubber cement. Samples were denatured at 78 °C
1031 on an inverted heat block for 3 minutes, then incubated in a humidified chamber at 42°C for 16
1032 hours. Samples were then removed from the glass slides and washed twice to 60 °C with pre-
1033 warmed 2x SSC for 15 minutes, then washed twice with 0.4x SSC at room temperature for 15
1034 minutes. Finally, coverslips were mounted on glass slides with Vectashield mounting medium.
1035 DNA FISH samples were imaged on the same microscope as described above for
1036 immunofluorescence and RNA FISH. Z-stack images were collected from all the way below the
1037 focal plane to all the way above the focal plane, with a step size of 100 nm. All samples were
1038 imaged on the same day using the same illumination and acquisition settings to minimize
1039 coverslip to coverslip differences.

1040 **Analysis of Immunofluorescence, RNA, and DNA FISH**

1041 All cells were analyzed using a custom built Matlab script. First, a single image for each
1042 color channel was generated by automatically identifying the focal plane of the stack, and then
1043 integrating the pixel intensity for all pixels 1 µm above and below the focal plane. Nuclei were
1044 automatically segmented, but replication compartments could not reliable by detected using
1045 simple thresholding, and so each was manually annotated. A region of the image was selected to
1046 represent the black background, and the mean pixel value of this region was subtracted from
1047 every pixel in the image. After segmentation, the pixel values for each nucleus were recorded, as
1048 well as every RC within a given nucleus, and these were used to measure the signal within the
1049 RC, as well as the fraction of signal within compared to the rest of the nucleus
1050 (immunofluorescence only).

1051 **Quantification of DNA content within RCs**

1052 DNA FISH data were compared with ATAC-seq data for the 6 hpi timepoint. Despite the fact
1053 that U2OS are hypertriploid, we based all the calculations on the DNA content of a diploid cell.
1054 As such, the values presented here likely represent an upper bound on the relative concentrations
1055 of host and HSV1 gDNA for our experiments. Precise volume measurements for nuclei were
1056 based on data from Monier et al., 2000, volumetric measurements for RCs were taken directly
1057 from the annotations of the DNA FISH data. Measurement uncertainty was propagated following
1058 standard practices outlined in Taylor, 1997.

1059 **PALM of Pol II in RCs**

1060 For PALM experiments to precisely localize Pol II molecules within RCs, cells were labeled
1061 with 500 nM PA-JF_{549}, and then infected as described above. Cells were fixed in 4%
1062 Paraformaldehyde in PBS, washed twice with PBS. Fluorescent 100 nm and 200 nmTetraspek
1063 beads were mixed in a 9:1 ratio then diluted 1000-fold in PBS. 100 µL was added to each
1064 coverslip and allowed to settle for 5 minutes, followed by 5 minutes of washing while rocking.

1065 Coverslips were mounted in Attofluor Cell Chambers and covered with PALM imaging buffer
1066 (50 mM NaCl, 50 mM Tris pH 7.9, 2 mM Trolox) to reduce triplet-state blinking.
1067 Samples were imaged on a custom-built Nikon Ti microscope equipped similarly to the
1068 microscope for single particle tracking, with some differences described here. An Adaptive
1069 Optics module (MicAO) and a removable cylindrical lens were placed in the light path ahead of
1070 the EM-CCD (Andor iXon Ultra 897) cameras in the left and right camera ports (respectively) of
1071 the microscope. Astigmatism for precise 3D localization was introduced using the Adaptive
1072 Optics system. The Adaptive Optics system was controlled through the MicAO software and
1073 calibrated on 200 nM Tetraspek beads based on the total photon yield and point spread function
1074 shape after iterative tuning of the deformable mirror. After optimization, a slight astigmatism in
1075 the vertical Zernike mode (Astigmatism 90° = 0.060) was added, and several z-stacks of 100 nM
1076 Tetraspek beads with 10 nm between slices to calibrate the PSF shape with the Z-position.
1077 30,000 frames were acquired with the 561 nm laser line and increasing amounts of 405 nm
1078 illumination in order to keep the number of single molecules consistent across the duration of
1079 acquisition.
1080 Spatial statistics were collected on cells using previously published methods (Boehning et al.,
1081 2018). First, cell boundaries and replication compartments were annotated as for spaSPT
1082 experiments (above). Particularly for small objects like RCs, edge correction is crucial for
1083 accurate spatial point pattern statistics. Given a set of detections P, we used the estimator *f* to
1084 correct for biases generated by points near the RC boundary:

1085 $$f(i,j,r) = \begin{cases} 0, & if\ d(i,j) > r \\ \dfrac{2\pi\, d(i,j)}{C_{in}}, & otherwise \end{cases}$$

1086 where *d(i,j)* is the distance between points *i* and *j* for $i,j \in P$, and C_{in} is arclength of the part of
1087 the circle of *d(i,j)* centered on *i* which is inside the annotated region (Goreaud and Pélissier,
1088 1999). We then calculated N(r), the local neighborhood density:

1089 $$N(r) = \frac{1}{N_p} \sum_{i \in P} \sum_{i \neq j} f(i,j,r)$$

1090 where N_p is the total number of detections within the region (Goreaud and Pélissier, 1999).
1091 The modified L-function is compared to complete spatial randomness (CSR), a homogenous
1092 Poisson process with intensity λ, equal to the density of detections in the region of interest A.
1093 The K-Ripley function is defined as:

1094 $$K(r) = \frac{N(r)}{\lambda}$$

1095 (Ripley, 1977). We estimated the modified L-function given by:

1096 $$L(r) - r = \sqrt{\frac{K(r)}{\pi}} - r$$

1097 (Goreaud and Pélissier, 1999). For the modified L-function, a spatial distribution with CSR
1098 remains at 0 for all radii. To implement this analysis, we used a previously published python
1099 script and the ADS R package to estimate the spatial statistics (Boehning et al., 2018; Pélissier
1100 and Goreaud, 2015). In order to estimate the error in our measurements, for each cell we
1101 performed random subsampling of the data, before annotation, to randomly select 25,000
1102 detections 100 times, and fed these subsampled data to the R script computing the statistic.

1103 **STORM on infected cells**

1104 For STORM experiments to visualize both RNA Polymerase II and the viral DNA, U2OS
1105 cells stably expressing Halo-RPB1 were plated on coverslips, labeled with 300 nM JF_{549}, and
1106 infected with the UL2/50 virus strain (Dembowski and DeLuca, 2015) as described above. After
1107 infection incubation with virus, cells were transferred into complete medium containing 300
1108 µg/mL PAA for two hours to prevent replication. After two hours, cells were released from
1109 inhibition by exchanging the culture medium with complete medium containing 2.5 µM 5-
1110 Ethynyldeoxyuridine for 4 hours. Cells were fixed with 4% Paraformaldehyde in PBS for 10
1111 minutes, then permeabilized with 0.5% Triton X100 in PBS for 10 minutes. Copper(1)-catalyzed
1112 alkyne-azide cycloaddition was performed with the ClickIT imaging kit following the
1113 manufacturer's protocol (Thermo). Coverslips were mounted in Attofluor Cell Chambers and
1114 covered with freshly-made STORM buffer (50 mM NaCl, 50 mM Tris pH 7.9, 10% D-glucose,
1115 10 mM DTT, 700 µg/mL Glucose Oxidase (Sigma), and 4 µg/mL catalase). STORM
1116 experiments were performed on the same microscope described for PALM.

1117 **Data and Software Availability**

1118 The GEO accession number for the ATAC-seq data is: **GSE117335**. The SPT trajectory data
1119 are available via Zenodo at DOI:10.5281/zenodo.1313872. The software used to generate these
1120 data is available at https://gitlab.com/tjian-darzacq-lab.

1121 **References**

1122 Abrisch, R.G., Eidem, T.M., Yakovchuk, P., Kugel, J.F., and Goodrich, J.A. (2015). Infection by
1123 Herpes Simplex Virus Type-1 Causes Near-Complete Loss of RNA Polymerase II
1124 Occupancy on the Host Cell Genome. J. Virol. JVI.02665-15.

1125 Alekseev, S., Nagy, Z., Sandoz, J., Weiss, A., Egly, J., Le May, N., and Coin, F. (2017).
1126 Transcription without XPB Establishes a Unified Helicase-Independent Mechanism of
1127 Promoter Opening in Eukaryotic Gene Expression. Mol. Cell *65*, 504–514.e4.

1128 Amitai, A. (2018). Chromatin Configuration Affects the Dynamics and Distribution of a
1129 Transiently Interacting Protein. Biophys. J. *114*, 766–771.

1130 Annibale, P., Vanni, S., Scarselli, M., Rothlisberger, U., and Radenovic, A. (2011). Identification
1131 of clustering artifacts in photoactivated localization microscopy. Nat. Methods *8*, 527–528.

1132 Banani, S.F., Lee, H.O., Hyman, A.A., and Rosen, M.K. (2017). Biomolecular condensates:
1133 organizers of cellular biochemistry. Nat. Rev. Mol. Cell Biol. *18*, 285–298.

1134 Beliveau, B.J., Joyce, E.F., Apostolopoulos, N., Yilmaz, F., Fonseka, C.Y., McCole, R.B.,
1135 Chang, Y., Li, J.B., Senaratne, T.N., Williams, B.R., et al. (2012). Versatile design and
1136 synthesis platform for visualizing genomes with Oligopaint FISH probes. Proc. Natl. Acad.
1137 Sci. *109*, 21301–21306.

1138 Beliveau, B.J., Boettiger, A.N., Avendaño, M.S., Jungmann, R., McCole, R.B., Joyce, E.F., Kim-
1139 Kiselak, C., Bantignies, F., Fonseka, C.Y., Erceg, J., et al. (2015). Single-molecule super-
1140 resolution imaging of chromosomes and in situ haplotype visualization using Oligopaint
1141 FISH probes. Nat. Commun. *6*, 7147.

1142 Berg, O.G., Winter, R.B., and von Hippel, P.H. (1981). Diffusion-Driven Mechanisms of Protein

1143 Translocation on Nucleic Acids. 1. Models and Theory. Biochemistry *20*, 6929–6948.

1144 Bergeron-Sandoval, L.-P., Safaee, N., and Michnick, S.W. (2016). Mechanisms and
1145 Consequences of Macromolecular Phase Separation. Cell *165*, 1067–1079.

1146 Betzig, E., Patterson, G.H., Sougrat, R., Lindwasser, O.W., Olenych, S., Bonifacino, J.S.,
1147 Davidson, M.W., Lippincott-Schwartz, J., and Hess, H.F. (2006). Imaging intracellular
1148 fluorescent proteins at nanometer resolution. Science *313*, 1642–1645.

1149 Blaho, J.A., Morton, E.R., and Yedowitz, J.C. (2005). Herpes Simplex Virus: Propagation,
1150 Quantification, and Storage. Curr. Protoc. Microbiol. 0–23.

1151 Bloom, D.C., Giordani, N. V., and Kwiatkowski, D.L. (2010). Epigenetic regulation of latent
1152 HSV-1 gene expression. Biochim. Biophys. Acta - Gene Regul. Mech. *1799*, 246–256.

1153 Boehning, M., Dugast-Darzacq, C., Rankovic, M., Hansen, A.S., Yu, T.-K., Marie-Nelly, H.,
1154 Kokic, G., Dailey, G.M., Cramer, P., Darzacq, X., et al. (2018). RNA polymerase II
1155 clustering through CTD phase separation. BioRxiv.

1156 Boettiger, A.N., Bintu, B., Moffitt, J.R., Wang, S., Beliveau, B.J., Fudenberg, G., Imakaev, M.,
1157 Mirny, L.A., Wu, C., and Zhuang, X. (2016). Super-resolution imaging reveals distinct
1158 chromatin folding for different epigenetic states. Nature *529*, 418–422.

1159 Bolintineanu, D.S., Volzing, K., Vivcharuk, V., Sayyed-Ahmad, A., Srivastava, P., and
1160 Kaznessis, Y.N. (2014). Investigation of Changes in Tetracycline Repressor Binding upon
1161 Mutations in the Tetracycline Operator. J. Chem. Eng. Data *59*, 3167–3176.

1162 Brangwynne, C.P., Mitchison, T.J., and Hyman, A.A. (2011). Active liquid-like behavior of
1163 nucleoli determines their size and shape in Xenopus laevis oocytes. Proc. Natl. Acad. Sci.
1164 *108*, 4334–4339.

1165 Buenrostro, J.D., Giresi, P.G., Zaba, L.C., Chang, H.Y., and Greenleaf, W.J. (2013).
1166 Transposition of native chromatin for fast and sensitive epigenomic profiling of open
1167 chromatin, DNA-binding proteins and nucleosome position. Nat. Methods *10*, 1213–1218.

1168 Chang, L., Godinez, W.J., Kim, I.-H., Tektonidis, M., de Lanerolle, P., Eils, R., Rohr, K., and
1169 Knipe, D.M. (2011). Herpesviral replication compartments move and coalesce at nuclear
1170 speckles to enhance export of viral late mRNA. Proc. Natl. Acad. Sci. U. S. A. *108*, E136–
1171 E144.

1172 Chao, S.H., and Price, D.H. (2001). Flavopiridol Inactivates P-TEFb and Blocks Most RNA
1173 Polymerase II Transcription in Vivo. J. Biol. Chem. *276*, 31793–31799.

1174 Chen, F., Gao, X., Shilatifard, A., and Shilatifard, A. (2015). Stably paused genes revealed
1175 through inhibition of transcription initiation by the TFIIH inhibitor triptolide. Genes Dev. *29*,
1176 39–47.

1177 Chen, J., Zhang, Z., Li, L., Chen, B.-C., Revyakin, A., Hajj, B., Legant, W., Dahan, M., Lionnet,
1178 T., Betzig, E., et al. (2014). Single-molecule dynamics of enhanceosome assembly in
1179 embryonic stem cells. Cell *156*, 1274–1285.

1180 Cho, W.-K., Spille, J.-H., Hecht, M., Lee, C., Li, C., Grube, V., and Cisse, I.I. (2018). Mediator
1181 and RNA polymerase II clusters associate in transcription-dependent condensates. Science

1182 *4199*, eaar4199.

1183 Chong, S., Dugast-Darzacq, C., Liu, Z., Dong, P., Dailey, G.M., Cattoglio, C., Heckert, A.,
1184 Banala, S., Lavis, L., Darzacq, X., et al. (2018). Imaging dynamic and selective low-
1185 complexity domain interactions that control gene transcription. Science *2555*, eaar2555.

1186 Cisse, I.I., Izeddin, I., Causse, S.Z., Boudarene, L., Senecal, A., Muresan, L., Dugast-Darzacq,
1187 C., Hajj, B., Dahan, M., and Darzacq, X. (2013). Real-time dynamics of RNA polymerase II
1188 clustering in live human cells. Science *341*, 664–667.

1189 Cortini, R., and Filion, G.J. (2018). Theoretical principles of transcription factor traffic on folded
1190 chromatin. Nat. Commun. *9*, 1740.

1191 Courchaine, E.M., Lu, A., and Neugebauer, K.M. (2016). Droplet organelles? EMBO J. *35*,
1192 1603–1612.

1193 Darzacq, X., Shav-Tal, Y., de Turris, V., Brody, Y., Shenoy, S.M., Phair, R.D., and Singer, R.H.
1194 (2007). In vivo dynamics of RNA polymerase II transcription. Nat. Struct. Mol. Biol. *14*,
1195 796–806.

1196 Davis, Z.H., Verschueren, E., Jang, G.M., Kleffman, K., Johnson, J.R., Park, J., Von Dollen, J.,
1197 Maher, M.C., Johnson, T., Newton, W., et al. (2015). Global Mapping of Herpesvirus-Host
1198 Protein Complexes Reveals a Transcription Strategy for Late Genes. Mol. Cell *57*, 349–360.

1199 Dembowski, J. a., and DeLuca, N.A. (2015). Selective Recruitment of Nuclear Factors to
1200 Productively Replicating Herpes Simplex Virus Genomes. PLOS Pathog. *11*, e1004939.

1201 Dosztanyi, Z., Csizmok, V., Tompa, P., and Simon, I. (2005). IUPred: web server for the
1202 prediction of intrinsically unstructured regions of proteins based on estimated energy content.
1203 Bioinformatics *21*, 3433–3434.

1204 Dosztányi, Z., Csizmók, V., Tompa, P., and Simon, I. (2005). The pairwise energy content
1205 estimated from amino acid composition discriminates between folded and intrinsically
1206 unstructured proteins. J. Mol. Biol. *347*, 827–839.

1207 Eriksson, B.F., and Schinazi, R.F. (1989). Combinations of 3'-azido-3'-deoxythymidine
1208 (zidovudine) and phosphonoformate (foscarnet) against human immunodeficiency virus type
1209 1 and cytomegalovirus replication in vitro. Antimicrob. Agents Chemother. *33*, 663–669.

1210 Everett, R.D. (2000). ICP0, a regulator of herpes simplex virus during lytic and latent infection.
1211 Bioessays *22*, 761–770.

1212 Feric, M., Vaidya, N., Harmon, T.S., Mitrea, D.M., Zhu, L., Richardson, T.M., Kriwacki, R.W.,
1213 Pappu, R.V., and Brangwynne, C.P. (2016). Coexisting Liquid Phases Underlie Nucleolar
1214 Subcompartments. Cell *165*, 1686–1697.

1215 Goreaud, F., and Pélissier, R. (1999). On explicit formulas of edge effect correction for Ripley's
1216 K -function. J. Veg. Sci. *10*, 433–438.

1217 Grimm, J.B., English, B.P., Chen, J., Slaughter, J.P., Zhang, Z., Revyakin, A., Patel, R., Macklin,
1218 J.J., Normanno, D., Singer, R.H., et al. (2015). A general method to improve fluorophores for
1219 live-cell and single-molecule microscopy. Nat. Methods *12*.

1220 Grimm, J.B., English, B.P., Choi, H., Muthusamy, A.K., Mehl, B.P., Dong, P., Brown, T.A.,

1221 Lippincott-Schwartz, J., Liu, Z., Lionnet, T., et al. (2016). Bright photoactivatable
1222 fluorophores for single-molecule imaging. Nat. Methods *13*, 985–988.

1223 Hansen, A.S., Pustova, I., Cattoglio, C., Tjian, R., and Darzacq, X. (2017). CTCF and cohesin
1224 regulate chromatin loop stability with distinct dynamics. Elife *6*, 1–33.

1225 Hansen, A.S., Woringer, M., Grimm, J.B., Lavis, L.D., Tjian, R., and Darzacq, X. (2018).
1226 Robust model-based analysis of single-particle tracking experiments with Spot-On. Elife *7*,
1227 1–33.

1228 Hew, K., Dahlroth, S.-L., Nordlund, P., Cornvik, T., and Pan, L.X. (2015). VP22 core domain
1229 from Herpes simplex virus 1 reveals a surprising structural conservation in both the Alpha-
1230 and Gammaherpesvirinae subfamilies. J. Gen. Virol. *96*, 1436–1445.

1231 Hnisz, D., Shrinivas, K., Young, R.A., Chakraborty, A.K., and Sharp, P.A. (2017). A Phase
1232 Separation Model for Transcriptional Control. Cell *169*, 13–23.

1233 Hyman, A.A., Weber, C.A., and Jülicher, F. (2014). Liquid-Liquid Phase Separation in Biology.
1234 Annu. Rev. Cell Dev. Biol. *30*, 39–58.

1235 Izeddin, I., El Beheiry, M., Andilla, J., Ciepielewski, D., Darzacq, X., and Dahan, M. (2012).
1236 PSF shaping using adaptive optics for three-dimensional single-molecule super-resolution
1237 imaging and tracking. Opt. Express *20*, 4957.

1238 Izeddin, I., Récamier, V., Bosanac, L., Cisse, I.I., Boudarene, L., Dugast-Darzacq, C., Proux, F.,
1239 Bénichou, O., Voituriez, R., Bensaude, O., et al. (2014). Single-molecule tracking in live
1240 cells reveals distinct target-search strategies of transcription factors in the nucleus. Elife
1241 e02230.

1242 Jonkers, I., Kwak, H., and Lis, J.T. (2014). Genome-wide dynamics of Pol II elongation and its
1243 interplay with promoter proximal pausing, chromatin, and exons. Elife *2014*, 1–25.

1244 Knipe, D.M., and Cliffe, A. (2008). Chromatin control of herpes simplex virus lytic and latent
1245 infection. Nat. Rev. Microbiol. *6*, 211–221.

1246 Lang, F., Li, X., Vladimirova, O., Hu, B., Chen, G., Xiao, Y., Singh, V., Lu, D., Li, L., Han, H.,
1247 et al. (2017). CTCF interacts with the lytic HSV-1 genome to promote viral transcription.
1248 Sci. Rep. *7*, 39861.

1249 Langmead, B., and Salzberg, S.L. (2012). Fast gapped-read alignment with Bowtie 2. Nat.
1250 Methods *9*, 357–359.

1251 Lee, J.S., Raja, P., and Knipe, D.M. (2016). Herpesviral ICP0 Protein Promotes Two Waves of
1252 Heterochromatin Removal on an Early Viral Promoter during Lytic Infection. MBio *7*,
1253 e02007-15.

1254 Lester, J.T., and DeLuca, N.A. (2011). Herpes Simplex Virus 1 ICP4 Forms Complexes with
1255 TFIID and Mediator in Virus-Infected Cells. J. Virol. *85*, 5733–5744.

1256 Li, D., Fu, W., and Swaminathan, S. (2018). Continuous DNA replication is required for late
1257 gene transcription and maintenance of replication compartments in gammaherpesviruses.
1258 PLOS Pathog. *14*, e1007070.

1259 Lin, Y., Mori, E., Kato, M., Xiang, S., Wu, L., Kwon, I., and McKnight, S.L. (2016). Toxic PR

1260 Poly-Dipeptides Encoded by the C9orf72 Repeat Expansion Target LC Domain Polymers.
1261 Cell *167*, 789–802.e12.

1262 Los, G. V, Encell, L.P., McDougall, M.G., Hartzell, D.D., Karassina, N., Zimprich, C., Wood,
1263 M.G., Learish, R., Ohana, R.F., Urh, M., et al. (2008). HaloTag: A Novel Protein Labeling
1264 Technology for Cell Imaging and Protein Analysis. ACS Chem. Biol. *3*, 373–382.

1265 Lu, H., Yu, D., Hansen, A.S., Ganguly, S., Liu, R., Heckert, A., Darzacq, X., and Zhou, Q.
1266 (2018). Phase-separation mechanism for C-terminal hyperphosphorylation of RNA
1267 polymerase II. Nature *558*, 318–323.

1268 Mirny, L.A. (2010). Nucleosome-mediated cooperativity between transcription factors. Proc.
1269 Natl. Acad. Sci. *107*, 22534–22539.

1270 Mirny, L., Slutsky, M., Wunderlich, Z., Tafvizi, A., Leith, J., and Kosmrlj, A. (2009). How a
1271 protein searches for its site on DNA: the mechanism of facilitated diffusion. J. Phys. A Math.
1272 Theor. *42*, 434013.

1273 Monier, K., Armas, J.C., Etteldorf, S., Ghazal, P., and Sullivan, K.F. (2000). Annexation of the
1274 interchromosomal space during viral infection. Nat. Cell Biol. *2*, 661–665.

1275 Muylaert, I., and Elias, P. (2007). Knockdown of DNA ligase IV/XRCC4 by RNA interference
1276 inhibits herpes simplex virus type I DNA replication. J. Biol. Chem. *282*, 10865–10872.

1277 Nicovich, P.R., Owen, D.M., and Gaus, K. (2017). Turning single-molecule localization
1278 microscopy into a quantitative bioanalytical tool. Nat. Protoc. *12*, 453–461.

1279 Normanno, D., Boudarène, L., Dugast-Darzacq, C., Chen, J., Richter, C., Proux, F., Bénichou,
1280 O., Voituriez, R., Darzacq, X., and Dahan, M. (2015). Probing the target search of DNA-
1281 binding proteins in mammalian cells using TetR as model searcher. Nat. Commun. *6*, 7357.

1282 Pélissier, R., and Goreaud, F. (2015). ads Package for R: A Fast Unbiased Implementation of the
1283 K-function Family for Studying Spatial Point Patterns in Irregular-Shaped Sampling
1284 Windows. J. Stat. Softw. *63*.

1285 Persson, F., Lindén, M., Unoson, C., and Elf, J. (2013). Extracting intracellular diffusive states
1286 and transition rates from single-molecule tracking data. Nat. Methods *10*, 265–269.

1287 Pfoh, R., Lacdao, I.K., Georges, A.A., Capar, A., Zheng, H., Frappier, L., and Saridakis, V.
1288 (2015). Crystal Structure of USP7 Ubiquitin-like Domains with an ICP0 Peptide Reveals a
1289 Novel Mechanism Used by Viral and Cellular Proteins to Target USP7. PLoS Pathog. *11*, 1–
1290 23.

1291 Rajčáni, J., Andrea, V., and Ingeborg, R. (2004). Peculiarities of herpes simplex virus (HSV)
1292 transcription: An overview. Virus Genes *28*, 293–310.

1293 Rice, S. a, Long, M.C., Lam, V., and Spencer, C. a (1994). RNA polymerase II is aberrantly
1294 phosphorylated and localized to viral replication compartments following herpes simplex
1295 virus infection. J. Virol. *68*, 988–1001.

1296 Ripley, B.D. (1977). Modelling Spatial Patterns. J. R. Stat. Soc. Ser. B *39*, 172–212.

1297 Robinson, J.T., Thorvaldsdóttir, H., Winckler, W., Guttman, M., Lander, E.S., Getz, G., and
1298 Mesirov, J.P. (2011). Integrative genomics viewer. Nat. Biotechnol. *29*, 24–26.

1299 Rust, M.J., Bates, M., and Zhuang, X. (2006). Sub-diffraction-limit imaging by stochastic optical
1300 reconstruction microscopy (STORM). Nat. Methods *3*, 793–795.

1301 Rutkowski, A.J., Erhard, F., L'Hernault, A., Bonfert, T., Schilhabel, M., Crump, C., Rosenstiel,
1302 P., Efstathiou, S., Zimmer, R., Friedel, C.C., et al. (2015). Widespread disruption of host
1303 transcription termination in HSV-1 infection. Nat. Commun. *6*, 7126.

1304 Sabari, B.R., Dall'Agnese, A., Boija, A., Klein, I.A., Coffey, E.L., Shrinivas, K., Abraham, B.J.,
1305 Hannett, N.M., Zamudio, A. V, Manteiga, J.C., et al. (2018). Coactivator condensation at
1306 super-enhancers links phase separation and gene control. Science *3958*, eaar3958.

1307 Schmid, M., Speiseder, T., Dobner, T., and Gonzalez, R.A. (2014). DNA Virus Replication
1308 Compartments. J. Virol. *88*, 1404–1420.

1309 Shao, W., and Zeitlinger, J. (2017). Paused RNA polymerase II inhibits new transcriptional
1310 initiation. Nat. Genet. *49*, 1045–1051.

1311 Shin, Y., Berry, J., Pannucci, N., Haataja, M.P., Toettcher, J.E., and Brangwynne, C.P. (2017).
1312 Spatiotemporal Control of Intracellular Phase Transitions Using Light-Activated
1313 optoDroplets. Cell *168*, 159–171.e14.

1314 Strom, A.R., Emelyanov, A. V., Mir, M., Fyodorov, D. V., Darzacq, X., and Karpen, G.H.
1315 (2017). Phase separation drives heterochromatin domain formation. Nat. Publ. Gr. *547*, 241–
1316 245.

1317 Taylor, J.R. (1997). An Introduction to Error Analysis: The Study of Uncertainties in Physical
1318 Measurements (Sausalito, CA: University Science Books).

1319 Taylor, T.J., and Knipe, D.M. (2004). Proteomics of herpes simplex virus replication
1320 compartments: association of cellular DNA replication, repair, recombination, and chromatin
1321 remodeling proteins with ICP8. J. Virol. *78*, 5856–5866.

1322 Taylor, T.J., McNamee, E.E., Day, C., and Knipe, D.M. (2003). Herpes simplex virus replication
1323 compartments can form by coalescence of smaller compartments. Virology *309*, 232–247.

1324 Teves, S.S., An, L., Bhargava-Shah, A., Xie, L., Darzacq, X., and Tjian, R. (2018). A stable
1325 mode of bookmarking by TBP recruits RNA Polymerase II to mitotic chromosomes. Elife *7*.

1326 Thurman, R.E., Rynes, E., Humbert, R., Vierstra, J., Maurano, M.T., Haugen, E., Sheffield,
1327 N.C., Stergachis, A.B., Wang, H., Vernot, B., et al. (2012). The accessible chromatin
1328 landscape of the human genome. Nature *489*, 75–82.

1329 Titov, D. V., Gilman, B., He, Q.-L., Bhat, S., Low, W.-K., Dang, Y., Smeaton, M., Demain,
1330 A.L., Miller, P.S., Kugel, J.F., et al. (2011). XPB, a subunit of TFIIH, is a target of the
1331 natural product triptolide. Nat. Chem. Biol. *7*, 182–188.

1332 Torigoe, S.E., Urwin, D.L., Ishii, H., Smith, D.E., and Kadonaga, J.T. (2011). Identification of a
1333 Rapidly Formed Nonnucleosomal Histone-DNA Intermediate that Is Converted into
1334 Chromatin by ACF. Mol. Cell *43*, 638–648.

1335 Tunnicliffe, R.B., Schacht, M., Levy, C., Jowitt, T.A., Sandri-Goldin, R.M., and Golovanov,
1336 A.P. (2015). The structure of the folded domain from the signature multifunctional protein
1337 ICP27 from herpes simplex virus-1 reveals an intertwined dimer. Sci. Rep. *5*, 11234.

1338 Zhou, C., and Knipe, D.M. (2002). Association of herpes simplex virus type 1 ICP8 and ICP27
1339 proteins with cellular RNA polymerase II holoenzyme. J. Virol. *76*, 5893–5904.

1340

Figure 1

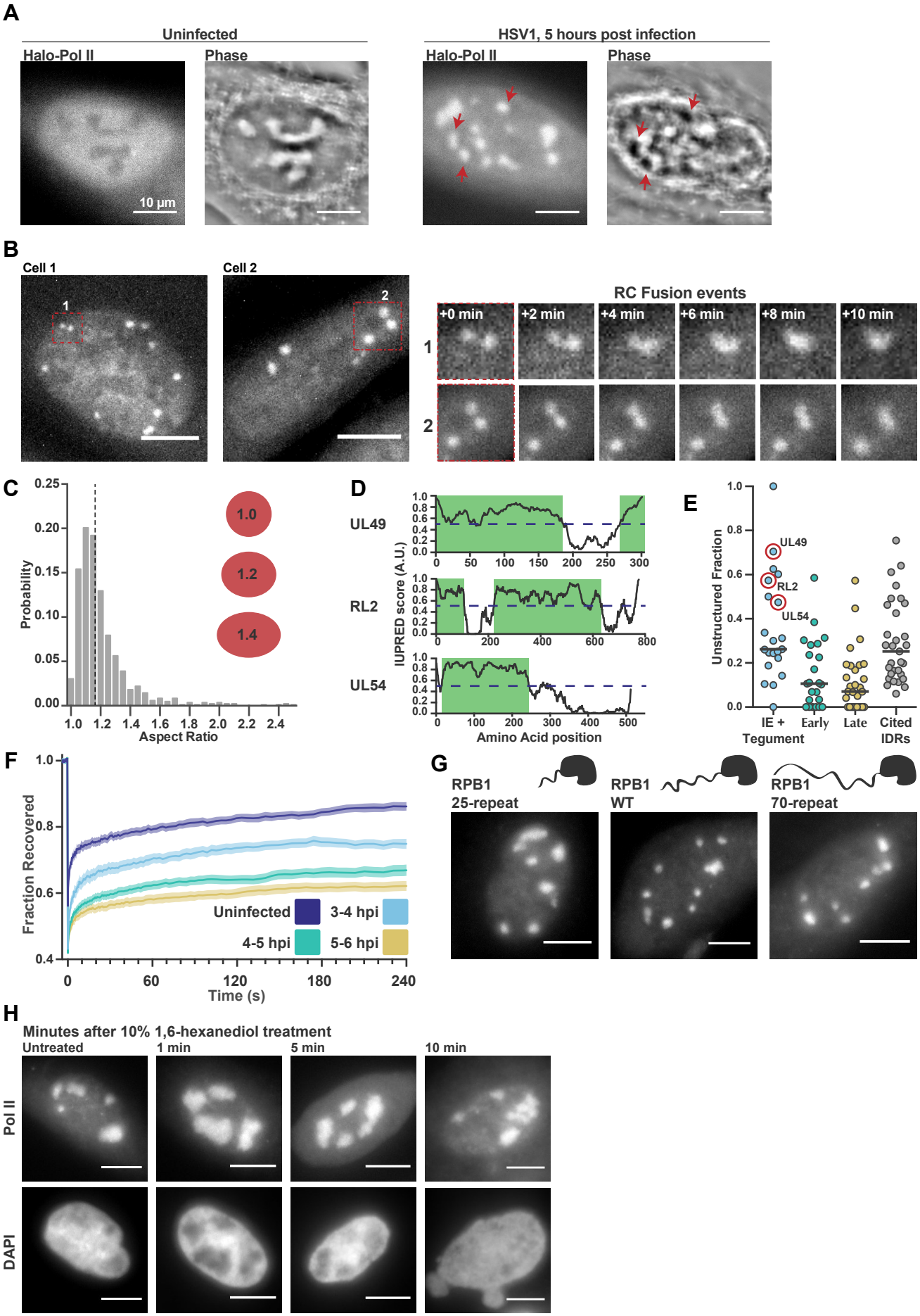
A
Uninfected
HSV1, 5 hours post infection
Halo-Pol II
Phase
10 µm
B
Cell 1
Cell 2
RC Fusion events
+0 min
+2 min
+4 min
+6 min
+8 min
+10 min
C
Probability
Aspect Ratio
1.0
1.2
1.4
D
UL49
RL2
UL54
IUPRED score (A.U.)
Amino Acid position
E
Unstructured Fraction
IE + Tegument
Early
Late
Cited IDRs
F
Fraction Recovered
Time (s)
Uninfected
3-4 hpi
4-5 hpi
5-6 hpi
G
RPB1 25-repeat
RPB1 WT
RPB1 70-repeat
H
Minutes after 10% 1,6-hexanediol treatment
Untreated
1 min
5 min
10 min
Pol II
DAPI

Figure 2

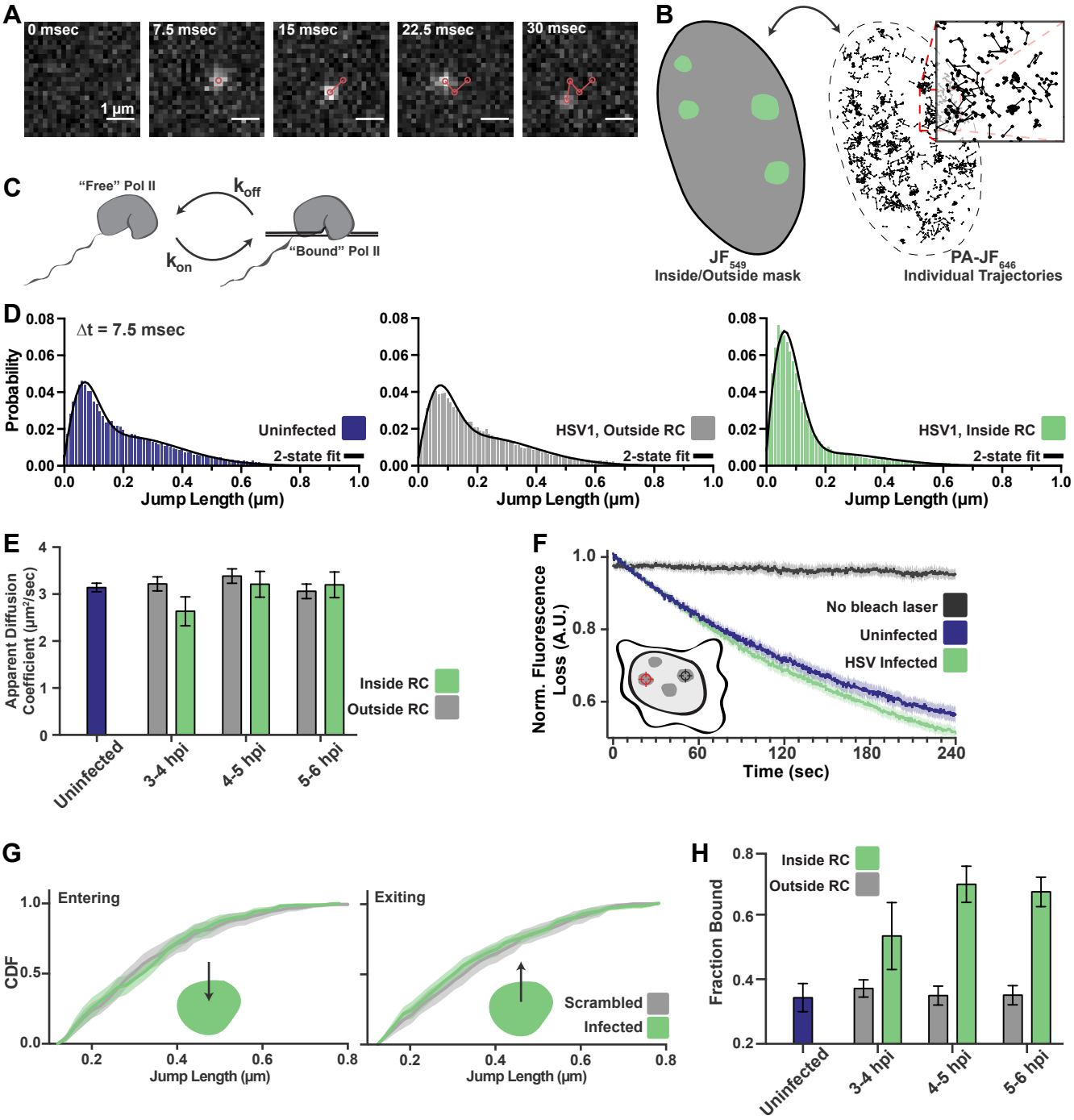
A
0 msec
7.5 msec
15 msec
22.5 msec
30 msec
1 µm
B
JF549
Inside/Outside mask
PA-JF646
Individual Trajectories
C
"Free" Pol II
"Bound" Pol II
koff
kon
D
Δt = 7.5 msec
Probability
Uninfected
HSV1, Outside RC
HSV1, Inside RC
2-state fit
Jump Length (µm)
E
Apparent Diffusion Coefficient (µm²/sec)
Inside RC
Outside RC
Uninfected
3-4 hpi
4-5 hpi
5-6 hpi
F
Norm. Fluorescence Loss (A.U.)
No bleach laser
Uninfected
HSV Infected
Time (sec)
G
Entering
Exiting
CDF
Scrambled
Infected
Jump Length (µm)
H
Fraction Bound
Inside RC
Outside RC
Uninfected
3-4 hpi
4-5 hpi
5-6 hpi

Figure 3

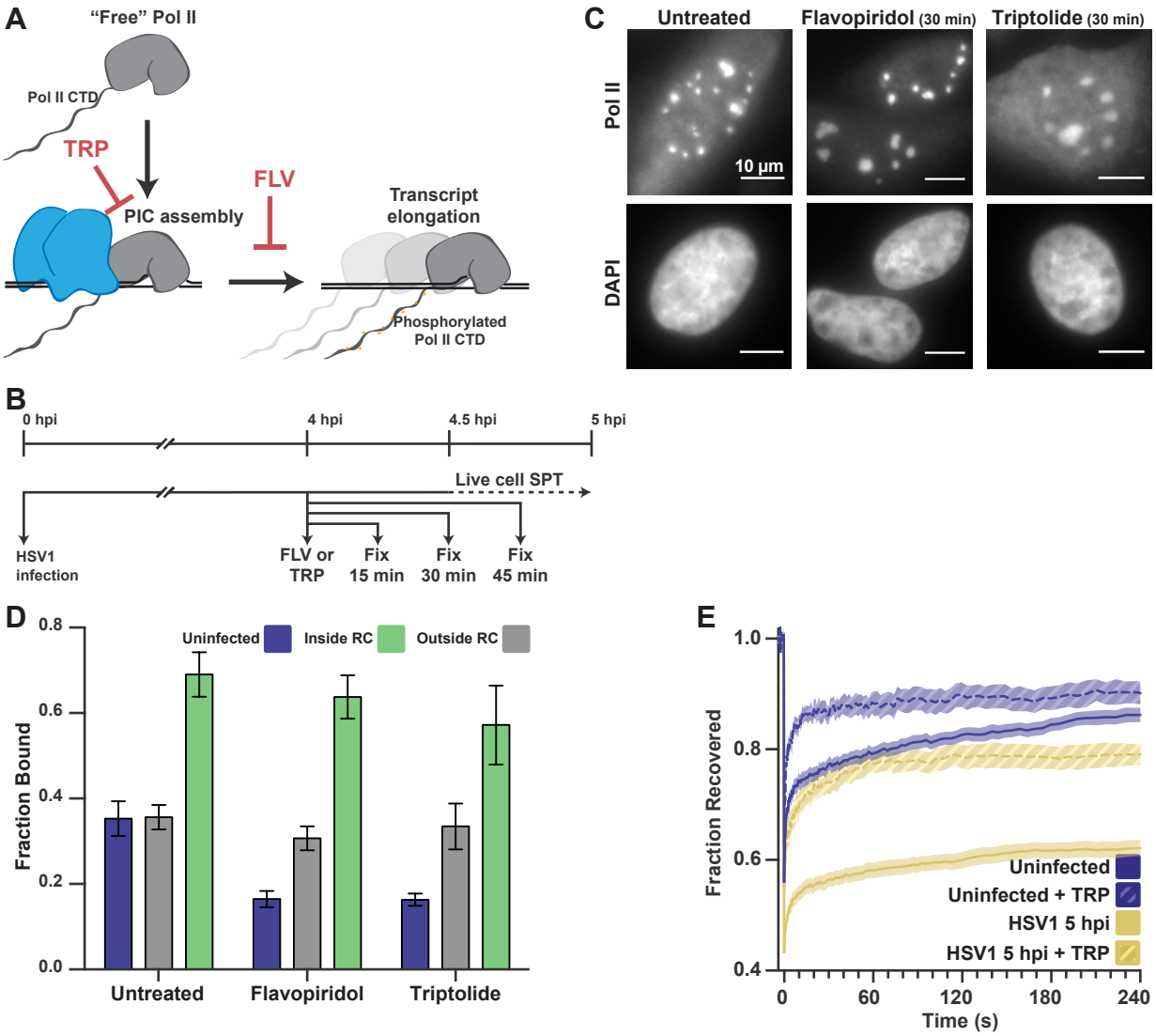
A
"Free" Pol II
Pol II CTD
TRP
PIC assembly
FLV
Transcript elongation
Phosphorylated Pol II CTD
C
Untreated
Flavopiridol (30 min)
Triptolide (30 min)
Pol II
DAPI
10 µm
B
0 hpi
4 hpi
4.5 hpi
5 hpi
Live cell SPT
HSV1 infection
FLV or TRP
Fix 15 min
Fix 30 min
Fix 45 min
D
Uninfected
Inside RC
Outside RC
Fraction Bound
0.0
0.2
0.4
0.6
0.8
Untreated
Flavopiridol
Triptolide
E
Fraction Recovered
1.0
0.8
0.6
0.4
Uninfected
Uninfected + TRP
HSV1 5 hpi
HSV1 5 hpi + TRP
0
60
120
180
240
Time (s)

Figure 4

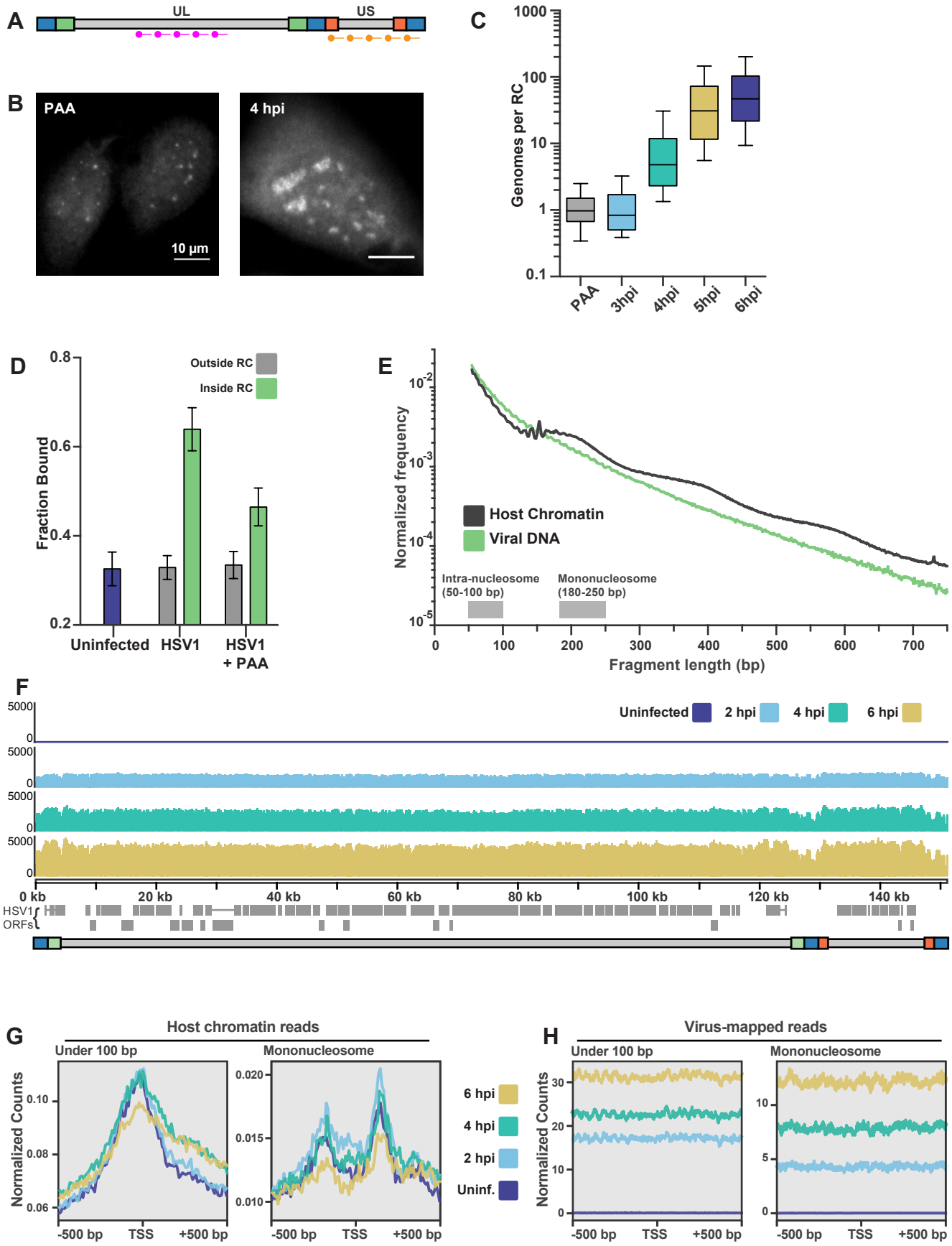
A
UL
US
B
PAA
4 hpi
10 µm
C
Genomes per RC
1000
100
10
1
0.1
PAA
3hpi
4hpi
5hpi
6hpi
D
Fraction Bound
0.8
0.6
0.4
0.2
Outside RC
Inside RC
Uninfected
HSV1
HSV1 + PAA
E
Normalized frequency
Host Chromatin
Viral DNA
Intra-nucleosome (50-100 bp)
Mononucleosome (180-250 bp)
Fragment length (bp)
0
100
200
300
400
500
600
700
F
Uninfected
2 hpi
4 hpi
6 hpi
5000
0
0 kb
20 kb
40 kb
60 kb
80 kb
100 kb
120 kb
140 kb
HSV1
ORFs
G
Host chromatin reads
Under 100 bp
Mononucleosome
Normalized Counts
-500 bp
TSS
+500 bp
6 hpi
4 hpi
2 hpi
Uninf.
H
Virus-mapped reads
Under 100 bp
Mononucleosome
Normalized Counts
-500 bp
TSS
+500 bp

Figure 5

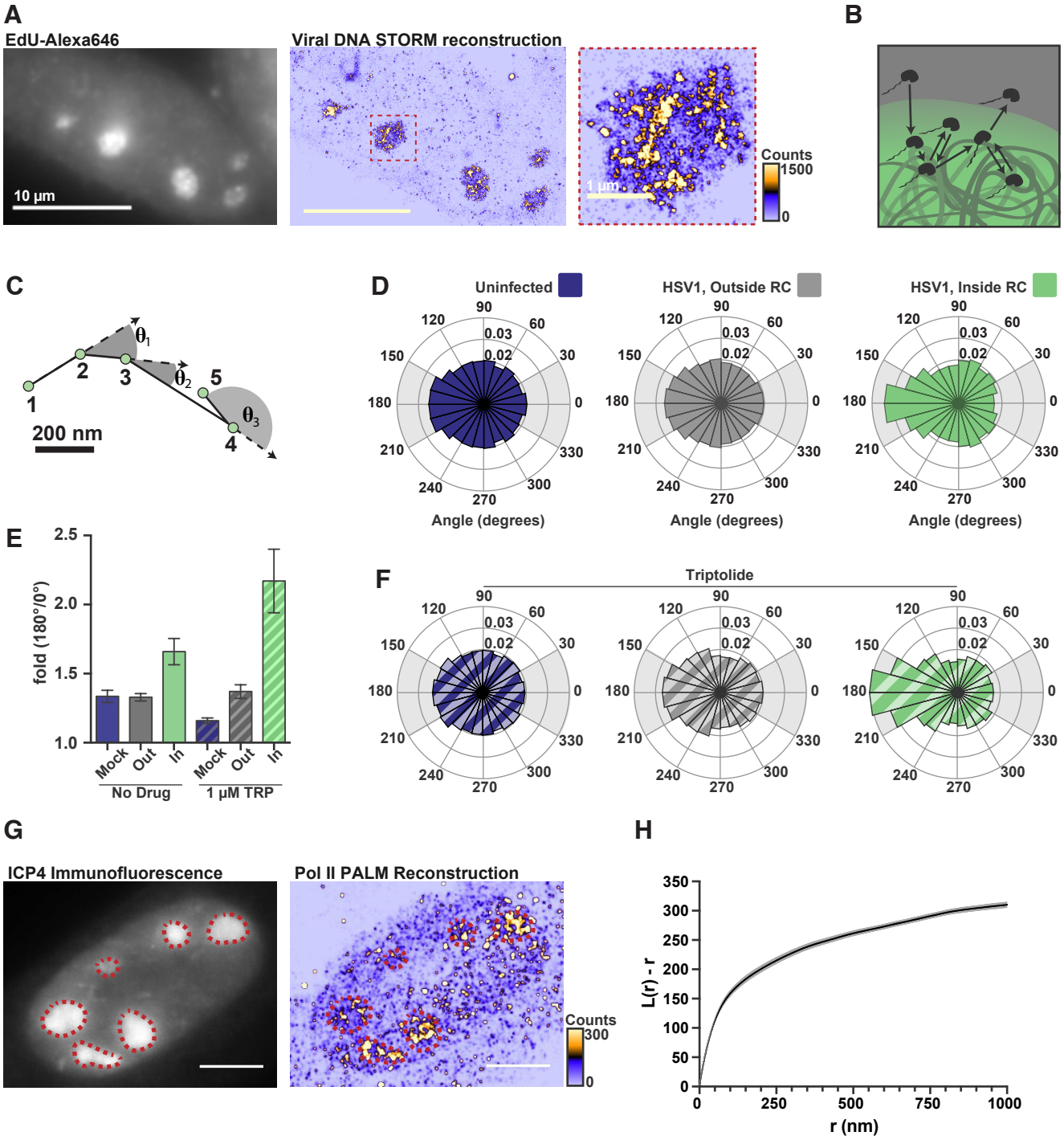
A
EdU-Alexa646
10 µm
Viral DNA STORM reconstruction
1 µm
Counts
1500
0
B
C
θ1
θ2
θ3
1
2
3
4
5
200 nm
D
Uninfected
HSV1, Outside RC
HSV1, Inside RC
0.03
0.02
Angle (degrees)
E
fold (180°/0°)
2.5
2.0
1.5
1.0
Mock
Out
In
No Drug
1 µM TRP
F
Triptolide
G
ICP4 Immunofluorescence
Pol II PALM Reconstruction
Counts
300
0
H
L(r) - r
r (nm)

Figure 6

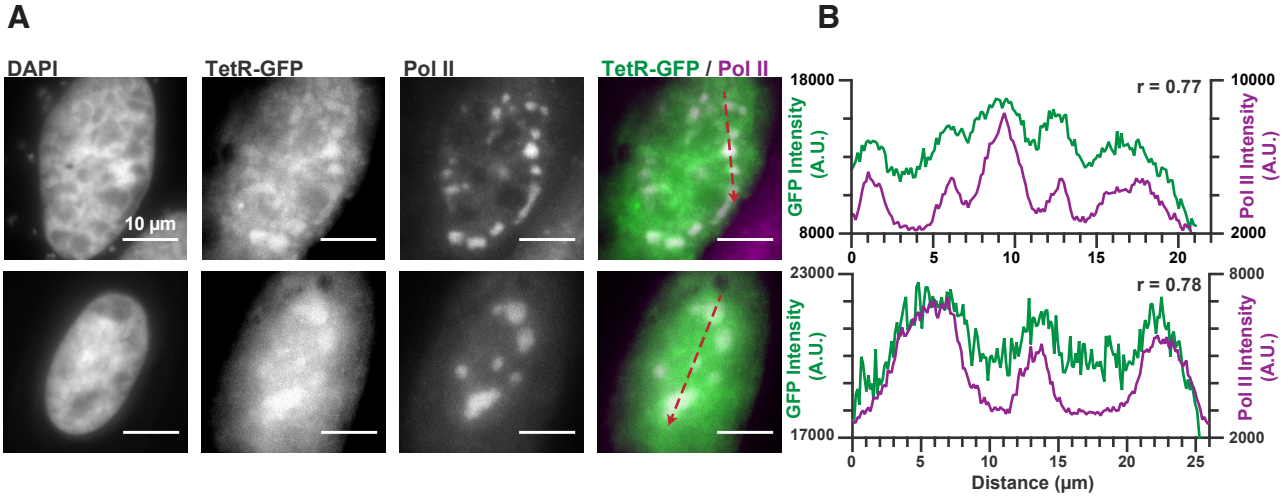
A
DAPI
TetR-GFP
Pol II
TetR-GFP / Pol II
10 µm
B
r = 0.77
GFP Intensity (A.U.)
Pol II Intensity (A.U.)
18000
8000
10000
2000
0
5
10
15
20
r = 0.78
23000
17000
8000
2000
25
Distance (µm)

Figure 7

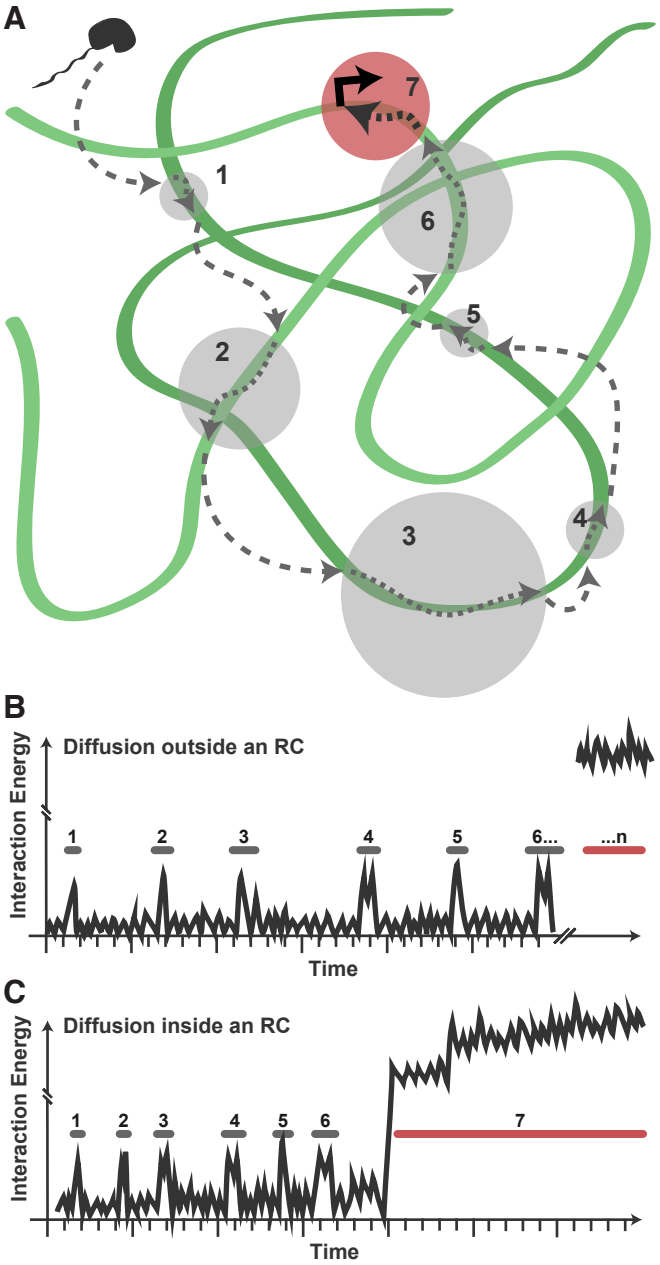
A
1
2
3
4
5
6
7
B
Diffusion outside an RC
Interaction Energy
1
2
3
4
5
6...
...n
Time
C
Diffusion inside an RC
Interaction Energy
1
2
3
4
5
6
7
Time

Figure S1

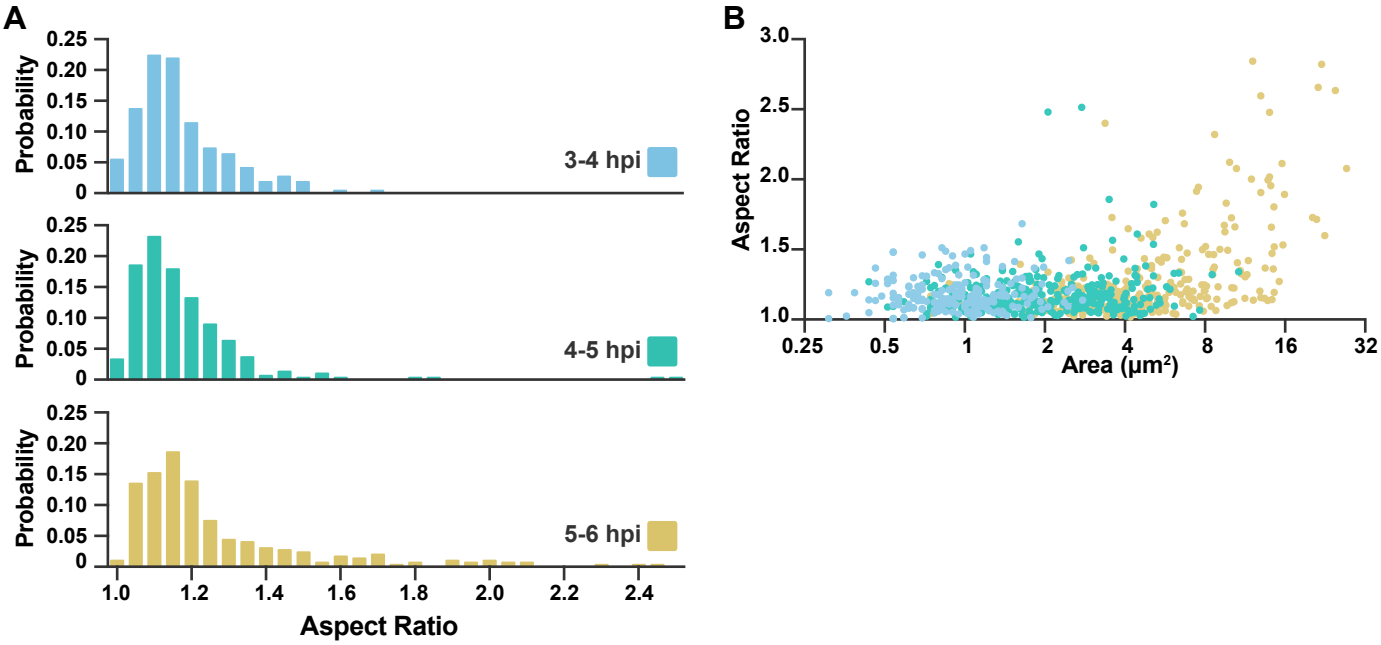
A
Probability
0.25
0.20
0.15
0.10
0.05
0
3-4 hpi
4-5 hpi
5-6 hpi
1.0
1.2
1.4
1.6
1.8
2.0
2.2
2.4
Aspect Ratio
B
Aspect Ratio
3.0
2.5
2.0
1.5
1.0
0.25
0.5
1
2
4
8
16
32
Area (μm²)

Figure S2

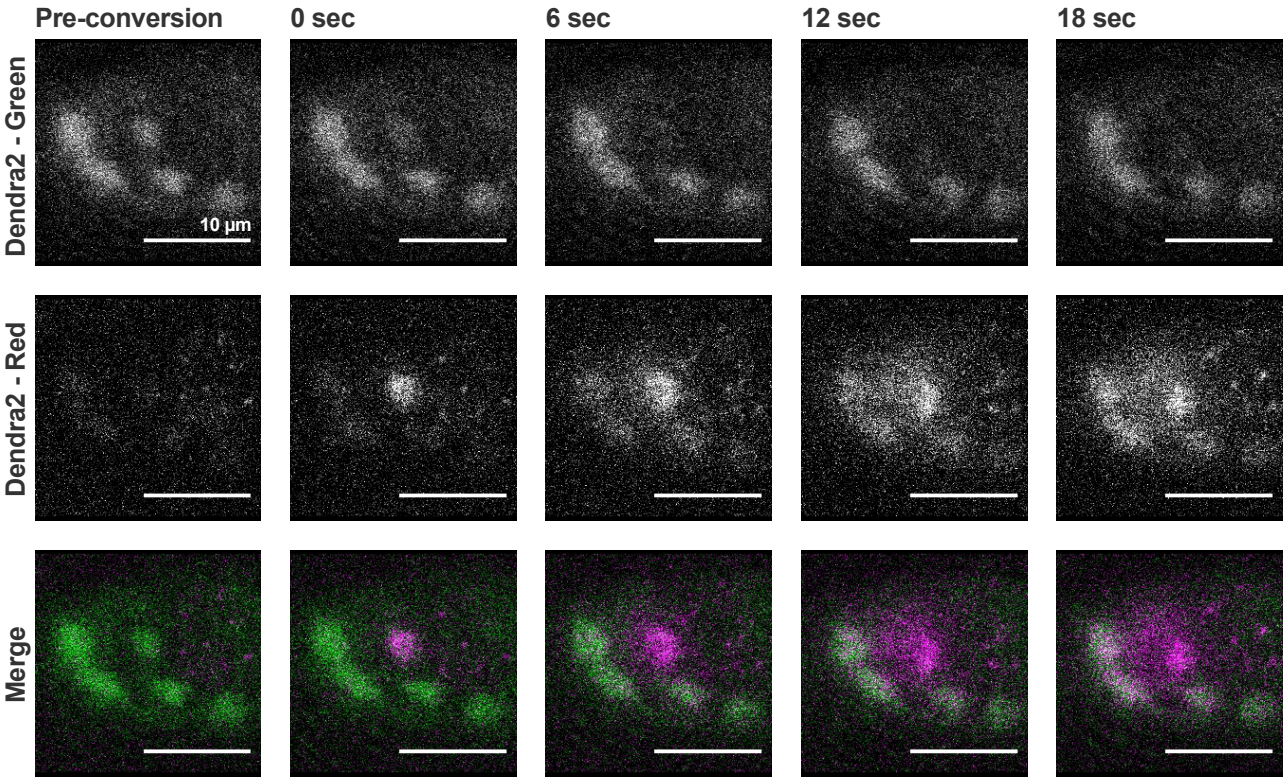
Pre-conversion
0 sec
6 sec
12 sec
18 sec
Dendra2 - Green
Dendra2 - Red
Merge
10 µm

Figure S3

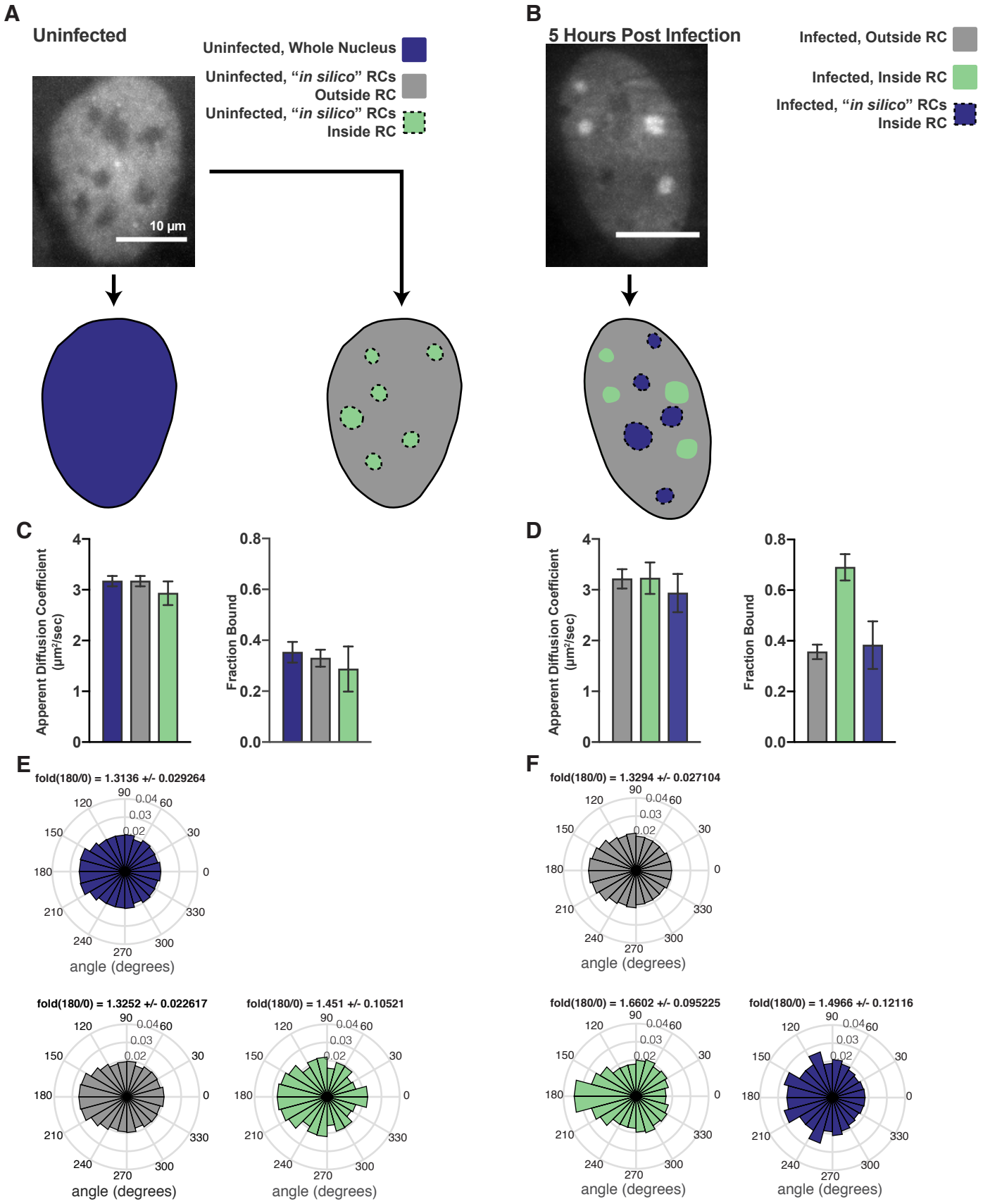
A
Uninfected
Uninfected, Whole Nucleus
Uninfected, "in silico" RCs Outside RC
Uninfected, "in silico" RCs Inside RC
10 µm
B
5 Hours Post Infection
Infected, Outside RC
Infected, Inside RC
Infected, "in silico" RCs Inside RC
C
Apperent Diffusion Coefficient (µm²/sec)
Fraction Bound
D
Apperent Diffusion Coefficient (µm²/sec)
Fraction Bound
E
fold(180/0) = 1.3136 +/- 0.029264
fold(180/0) = 1.3252 +/- 0.022617
fold(180/0) = 1.451 +/- 0.10521
angle (degrees)
F
fold(180/0) = 1.3294 +/- 0.027104
fold(180/0) = 1.6602 +/- 0.095225
fold(180/0) = 1.4966 +/- 0.12116
angle (degrees)

Figure S4

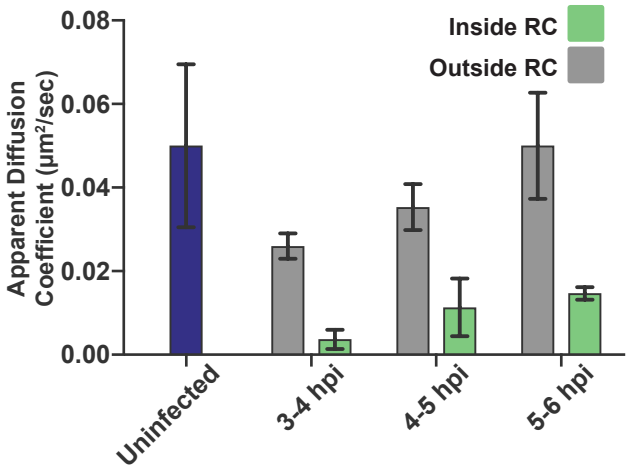
Inside RC
Outside RC
Apparent Diffusion Coefficient (μm²/sec)
0.08
0.06
0.04
0.02
0.00
Uninfected
3-4 hpi
4-5 hpi
5-6 hpi

Figure S5

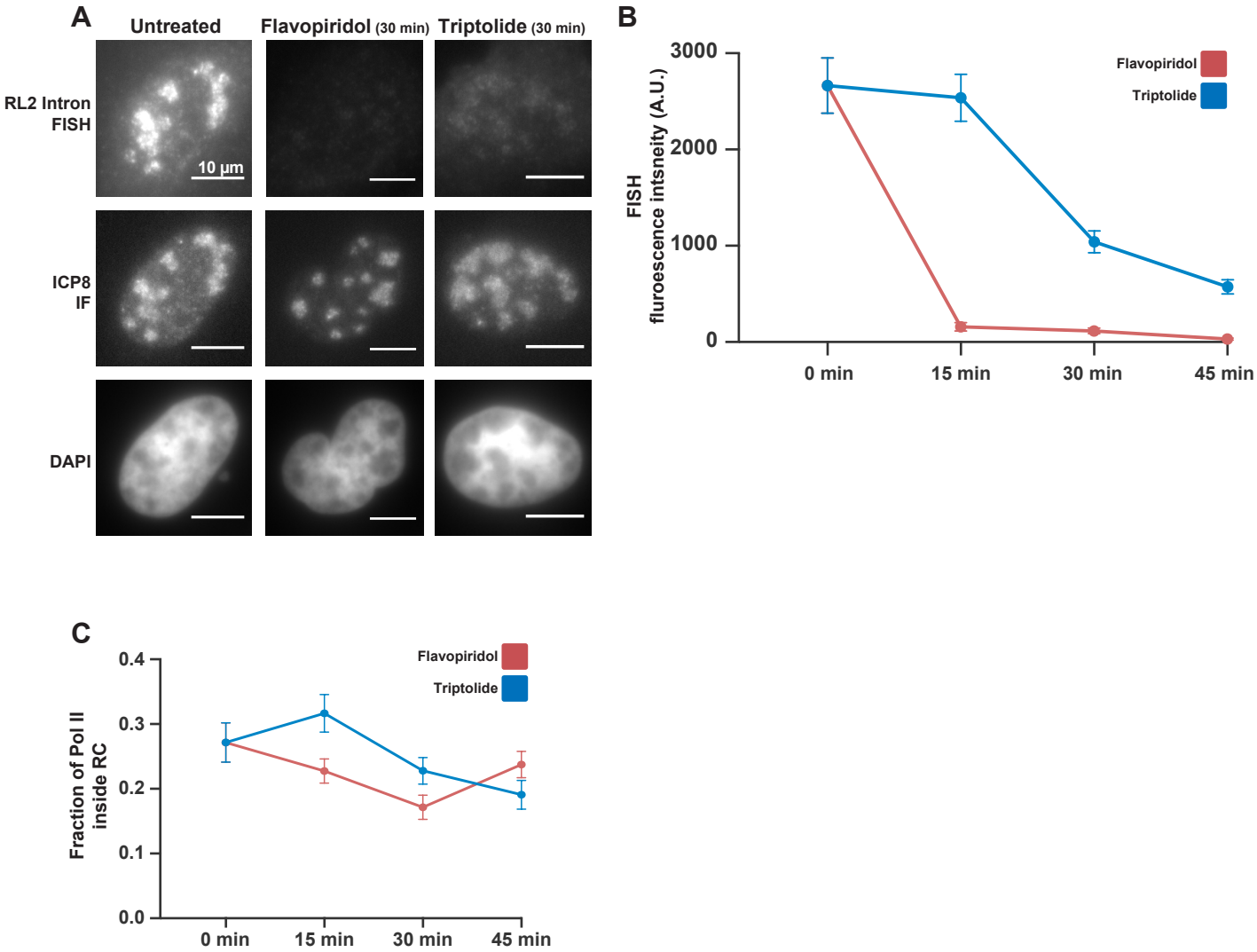
A
Untreated
Flavopiridol (30 min)
Triptolide (30 min)
RL2 Intron FISH
10 µm
ICP8 IF
DAPI
B
FISH fluroescence intsneity (A.U.)
3000
2000
1000
0
0 min
15 min
30 min
45 min
Flavopiridol
Triptolide
C
Fraction of Pol II inside RC
0.4
0.3
0.2
0.1
0.0
0 min
15 min
30 min
45 min
Flavopiridol
Triptolide

Figure S6

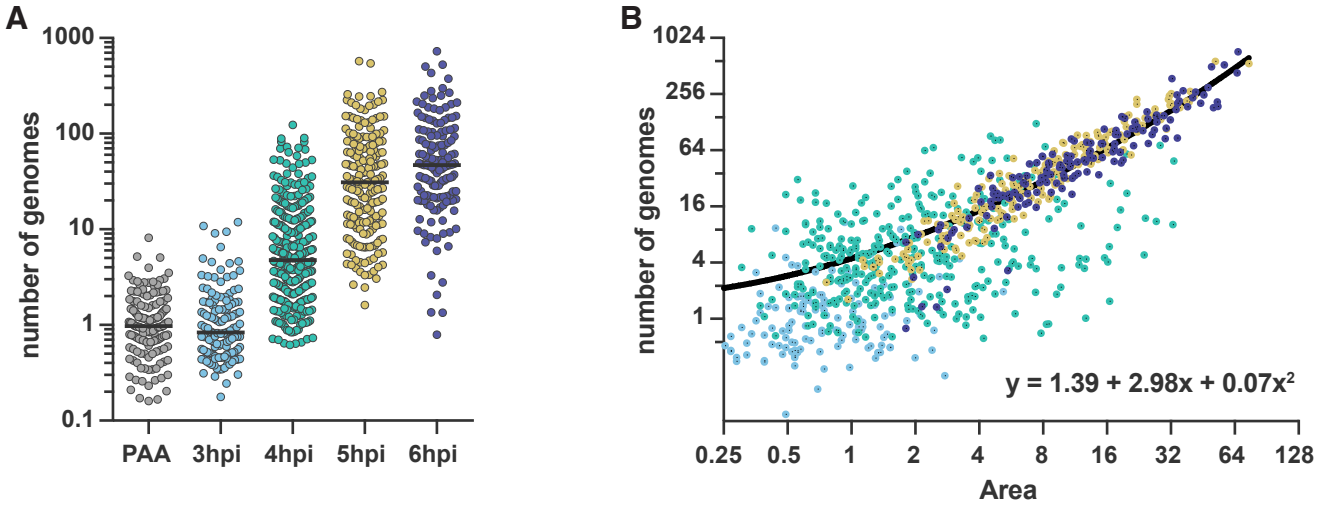
A
1000
100
10
1
0.1
number of genomes
PAA
3hpi
4hpi
5hpi
6hpi
B
1024
256
64
16
4
1
number of genomes
y = 1.39 + 2.98x + 0.07x²
0.25
0.5
1
2
4
8
16
32
64
128
Area

Figure S7

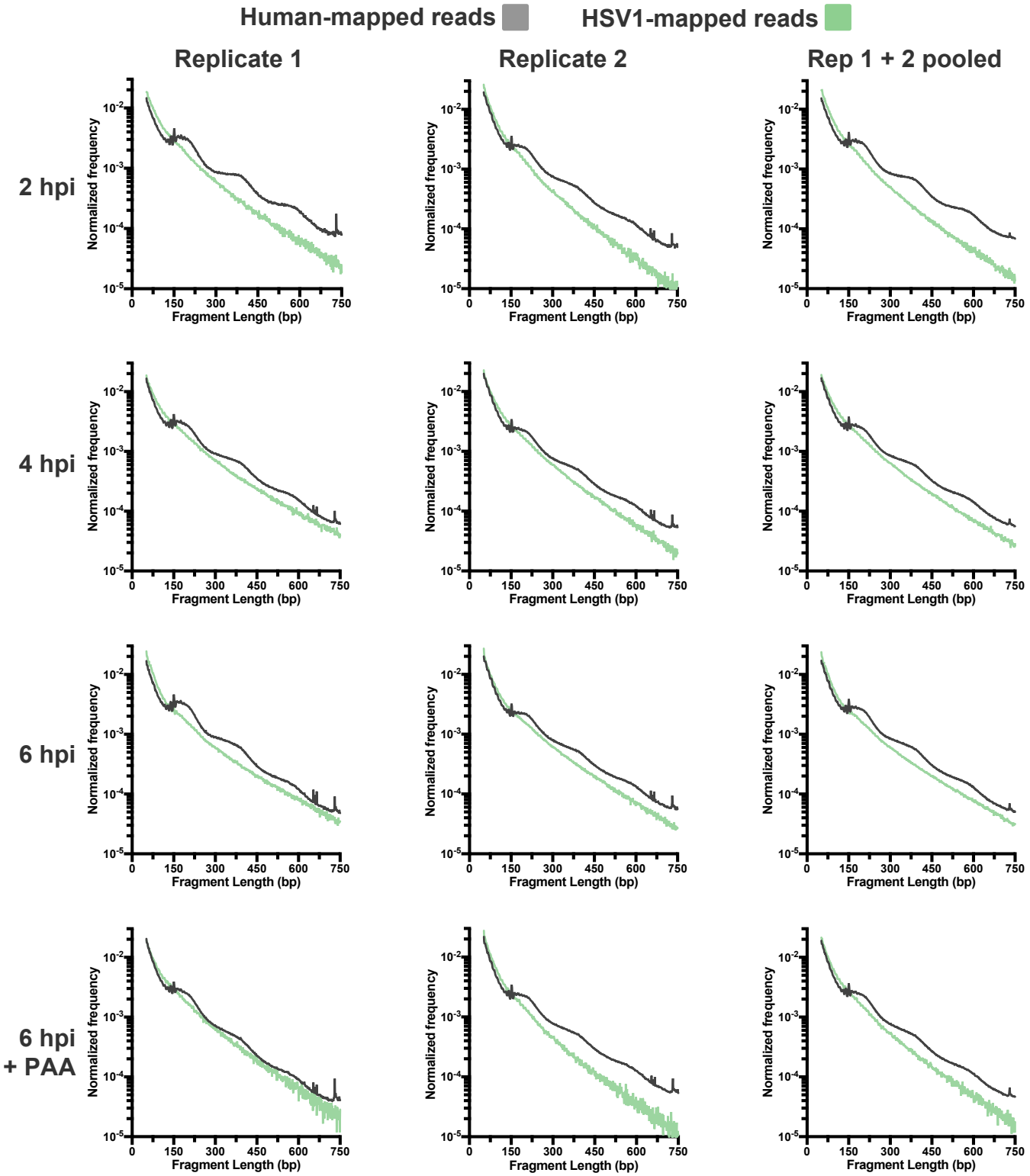
Human-mapped reads
HSV1-mapped reads
Replicate 1
Replicate 2
Rep 1 + 2 pooled
2 hpi
4 hpi
6 hpi
6 hpi + PAA
Normalized frequency
Fragment Length (bp)

Figure S8

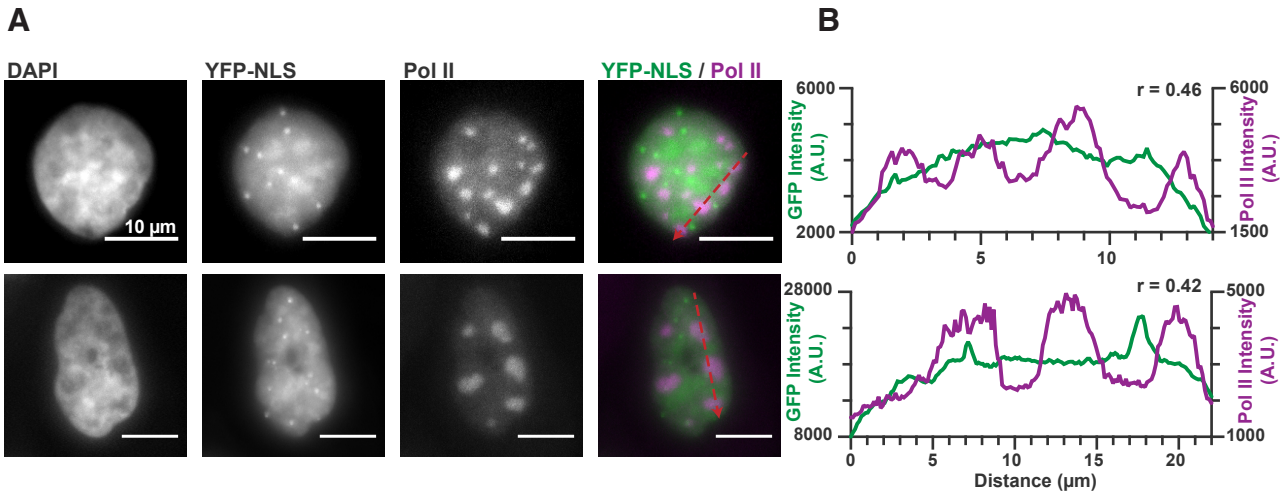
A
B
DAPI
YFP-NLS
Pol II
YFP-NLS / Pol II
10 µm
r = 0.46
r = 0.42
GFP Intensity (A.U.)
Pol II Intensity (A.U.)
6000
2000
1500
28000
8000
5000
1000
0
5
10
15
20
Distance (µm)

Table S1

gene name	function	Class	Protein Length	Region Start	Region End	IDR Length
RS1	transcription regulation	alpha	1294	0	79	79
				94	273	179
				594	615	21
				717	820	103
				884	893	9
				1214	1236	22
				1276	1294	18
US12	transcription regulation	alpha	88	35	88	53
US11	tegument	tegument	149	0	149	149
US10	tegument	tegument	300	23	92	69
				124	156	32
US9	membrane/glycoprotein	beta	57	0	16	16
				54	57	3
US8	membrane/glycoprotein	beta	190	0	5	5
				31	104	73
				172	190	18
US8A	membrane/glycoprotein	beta	550	161	215	54
				392	410	18
				480	550	70
US7	membrane/glycoprotein	beta	383	195	253	58
				325	383	58
US6	membrane/glycoprotein	beta	394	277	319	42
				381	394	13
US4	membrane/glycoprotein	gamma	239	33	170	137
US3	kinase/phosphatase	beta	481	19	170	151
US2	unknown	gamma	291	254	291	37
US1.5	unknown	alpha	250	0	10	10
				137	212	75
US1	replication	alpha	420	0	14	14
				15	181	166
				307	382	75
ICP0	transcription regulation	alpha	776	0	106	106
				222	568	346
				595	628	33
				761	776	15
UL56	membrane/glycoprotein	beta	234	0	101	101
				151	187	36
UL55	unknown	beta	186	179	186	7
UL54	transcription regulation	alpha	512	0	243	243
UL52	replication	beta	1058	0	12	12
				380	389	9
				480	497	17
				699	735	36
				1055	1058	3
UL51	tegument	tegument	244	180	244	64
UL50	replication	beta	371	0	7	7
				155	159	4
				333	371	38
UL49A	membrane/glycoprotein	beta	91	29	44	15
UL49	tegument	tegument	301	0	181	181
				270	301	31
UL48	transcription regulation	gamma	490	0	46	46
				454	456	2
				487	490	3

UL47	tegument	tegument	693	0	26	26
				51	125	74
				150	180	30
				680	693	13
UL46	tegument	tegument	719	0	8	8
				435	540	105
				561	606	45
				667	694	27
				706	719	13
UL45	membrane/glycoprotein	gamma	172	0	10	10
UL44	membrane/glycoprotein	gamma	511	39	125	86
				314	330	16
UL43	membrane/glycoprotein	gamma	415	0	17	17
				218	255	37
UL42	replication	beta	489	0	25	25
				333	448	115
				477	488	11
				110	148	38
UL41	tegument	tegument	489	286	367	81
UL40	replication	beta	340	0	13	13
UL39	replication	beta	1137	0	30	30
				125	157	32
				176	309	133
UL38	capsid	gamma	465	0	56	56
				70	85	15
				144	155	11
				357	388	31
UL37	tegument	tegument	1123	0	46	46
				971	977	6
				1057	1123	66
UL36	tegument	tegument	3136	0	22	22
				268	382	114
				396	495	99
				749	770	21
				948	971	23
				1254	1282	28
				1911	1925	14
				2267	2291	24
				2489	2534	45
				2553	2701	148
				2728	2984	256
				3029	3066	37
UL35	capsid	gamma	112	0	10	10
				40	46	6
				103	112	9
UL34	membrane/glycoprotein	gamma	275	0	11	11
UL33	packaging	gamma	130	0	14	14
UL32	packaging	gamma	596	0	5	5
				77	107	30
				227	237	10
UL31	other	gamma	306	0	41	41
UL30	replication	beta	1235	0	16	16
				50	61	11
				644	693	49
				1099	1134	35
				1233	1235	2
UL29	replication	beta	1196	0	8	8
				288	307	19
				1158	1196	38

UL28	packaging	gamma	785	265	288	23
				435	491	56
				778	785	7
UL27	membrane/glycoprotein	beta	904	45	99	54
				469	492	23
				819	836	17
				881	904	23
UL26.5	capsid	gamma	329	0	15	15
				108	171	63
				211	295	84
UL26	capsid	gamma	635	0	11	11
				270	318	48
				414	477	63
				517	601	84
UL25	packaging	gamma	580	108	132	24
UL24	unknown	gamma	269	0	3	3
				190	242	52
				265	269	4
UL23	replication	beta	376	0	41	41
				263	280	17
				371	376	5
UL22	membrane/glycoprotein	gamma	838	175	210	35
				293	317	24
UL21	tegument	tegument	535	206	231	25
				246	277	31
UL20	membrane/glycoprotein	gamma	222	0	10	10
UL19	capsid	gamma	1374	0	7	7
UL18	capsid	gamma	318	0	2	2
UL17	packaging	gamma	703	202	250	48
UL16	tegument	tegument	373	0	32	32
			373	154	175	21
UL15	packaging	gamma	735	0	3	3
UL14	tegument	tegument	219	0	7	7
				164	219	55
UL13	tegument	tegument	518	0	115	115
UL12	replication	beta	626	0	125	125
				603	626	23
UL11	tegument	tegument	96	48	96	48
UL10	membrane/glycoprotein	gamma	473	0	14	14
				366	427	61
				444	473	29
UL9	replication	beta	851	0	19	19
				263	283	20
UL7	tegument	tegument	296	0	6	6
UL6	capsid	gamma	676	0	17	17
				384	401	17
				629	676	47
UL5	replication	beta	882	0	34	34
				602	629	27
UL4	unknown	gamma	199	149	160	11
UL3	unknown	gamma	235	42	88	46
				144	158	14
				233	235	2
UL2	DNA repair	beta	334	0	94	94
UL1	membrane/glycoprotein	gamma	224	164	224	60
RL1	transcription regulation	late	240	0	130	130
				144	168	24
				236	240	4

Table S2

Protein	Organism[a]	Protein Length (AA)	Total IDR length (AA)	IDR Fraction	Reference[b]
FUS	Hs	526	397	0.75475285	Chong et al., 2018
Taf15	Hs	592	274	0.46283784	
EWS	Hs	656	420	0.6402439	
SP1	Hs	785	220	0.28025478	
Huntingtin	Hs	3142	311	0.09898154	Bergeron-Sandoval et al., 2016
PML	Hs	882	145	0.16439909	
PGL-1	Ce	730	94	0.12876712	
RPB1	Hs	1970	119	0.06040609	Boehning et al., 2018
DDX4	Hs	724	144	0.19889503	Courchaine et al., 2016
eIF4GII	Sc	907	229	0.25248071	
Fibrillarin	Hs	321	89	0.27725857	
hnRNPA1	Hs	320	48	0.15	
Laf1	Ce	708	232	0.32768362	
Lsm4	Sc	187	92	0.49197861	
RBM14	Hs	669	85	0.12705531	
SRSF2	Hs	221	135	0.61085973	
TDP-43	Hs	414	82	0.19806763	
Tia1	Hs	386	35	0.09067358	
Whi3	Ag	729	359	0.49245542	
PUB1	Hs	453	213	0.47019868	
HP1a	Dm	213	68	0.31924883	Strom et al., 2017
DAXX	Hs	740	407	0.55	Banani et al., 2017
PGL-3	Ce	693	124	0.17893218	
NPM1	Hs	294	125	0.42517007	
hRNPAB	Hs	332	93	0.28012048	Aguzzi and Altmeyer, 2016
hnRNPA3	Hs	378	56	0.14814815	
hnRNPA2B1	Hs	353	41	0.11614731	
hnRNPD	Hs	355	40	0.11267606	
hnRDL	Hs	420	127	0.30238095	
NUP145	Sc	1317	219	0.16628702	Schmidt and Görlich, 2015

a. Organism abbreviations: Hs, Homo sapiens; Ce, Caenorhabditis elegans; Sc, Saccharomyces cerevisiae; Dm, Drosophila melanogaster; Ag, Ashbya gossypii b. May include citations within reference.

Table S3

Table S3	Genome Size (bp)	Genome Copy number[c]	Total DNA (bp)	Percent of Total DNA[c]	Concentration (bp/µm^3)[d]	ATAC-seq read percentage[e]	Fold enrichment over expected[f]
Host Genome[a]	3.2 x10^9	2	6.4 x10^9	99.8 (± 0.2)	9.4 (± 1.6) x10^6	75.8 (± 10.4)	0.8 (± 0.1)
Viral DNA	1.5 x10^5	82 (± 105)	1.3 (± 1.6) x10^7	0.2 (± 0.2)	3.9 (± 5.8) x10^4	24.2 (± 10.4)	130 (± 170)
Rel. Diff.[b]	2.1 x10^4		513 (± 658)		240 (± 369)		

All values are the Mean (± S.D.).
a. Assuming karyotypically normal human cell; b. relative difference = Human / HSV1; c. Under experimental conditions of MOI = 1; d. Concentration assuming nucleus volume taken from Monier et al., 2000; e. based on total reads mapped from each organism, n = 3; f. Fold enrichment = ATAC-seq read percentage / Percent of Total DNA.